INVESTIGATIONS OF COHERENCE AND STRUCTURED LIGHT

by

Joseph R. Mays

A dissertation submitted to the faculty of
The University of North Carolina at Charlotte
in partial fulfillment of the requirements
for the degree of Doctor of Philosophy in
Optical Science and Optical Engineering

Charlotte

2023

Approved by:

_____
Dr. Gbur

_____
Dr. Allen

_____
Dr. Suleski

_____
Dr. Hasan

ABSTRACT

JOSEPH R. MAYS. Investigations of coherence and structured light. (Under the direction of DR. GBUR)

The combination of singular optics and partially coherent fields has become increasingly important in the applications of optical communication and optical imaging. Within this, we focus on the phenomena of optical vortices. We use and study the properties of these partially coherent vortex beams such as the total angular momentum, as well as investigate the effects of partial coherence on vortex created phenomena, namely superoscillations. In this dissertation we use the optical vortices as observed through the cross-spectral density in a partially coherent field to create superoscillations and investigate the superoscillatory behavior as the field is randomized. It is shown that a decrease in spatial coherence can in some cases strengthen the superoscillatory behavior, and in others decrease it. We then look at superoscillations that appear in the phase of the correlation function in partially coherent Talbot carpets. Utilizing the Talbot effect, it is shown that superoscillations can be propagated significant distances, even under a decrease in spatial coherence. It is also shown that this decrease in spatial coherence can strengthen the superoscillatory behavior at the primary and secondary Talbot images. We also introduce a modification to the class of partially coherent vortex beams known as Twisted Vortex Gaussian-Schell Model Beams through the addition of polarization. These beams have angular momentum from three different sources: the underlying vortex order of the beam, the "twist" given to the ensemble of beams, and the polarization of the beam. The combination of these angular momentum properties allows for unprecedented control over the total angular momentum of the field and its transverse distribution.

DEDICATION

This work is dedicated to my family and my cat Nugget. Thank you for always being a pillar I could lean on when times were hard. I also dedicate this to my mother. Her memory is a major driving factor for completing this work, and I wish she were still here to read this.

ACKNOWLEDGEMENTS

Foremost, I would like to express my sincere gratitude to my advisor Dr. Greg Gbur for the continuous support throughout my Ph.D. study and research. I thank him for his immense patience and valuable guidance. Under his advisement, I have grown beyond my own expectations of myself and will be able to use the lessons he has taught me for the rest of my life. Aside from my advisor, I would like to thank the rest of my thesis committee members: Dr. Angela Allen, Dr. Thomas Suleski, and Dr. Mohamad-Ali Hasan for their encouragement and insight. My sincere thanks also extend Dr. Subrata Sanyal and Dr. Joseph Fiordilino, as well as the SMART Scholarship program. None of this would have been possible without the unwavering support and encouragement I have received from them over the years.

TABLE OF CONTENTS

LIST OF FIGURES

LIST OF ABBREVIATIONS

AGSM Anisotropic Gaussian Schell-model

BC Beam Combiner

CL Cylindrical lens

FSOC Free Space Optical Communications

L Thin Lens

LG Laguerre-Gauss

M Mirror

OAM Orbital Angular Momentum

PBS Polarized Beam Splitter

QWP Quarter-Wave Plate

RGGP Rotating Ground Glass Plate

SAM Spin Angular Momentum

SLM Spatial Light Modulator

SPP Spiral Phase Plate

tGSM twisted Gaussian Schell-model

tvGSM twisted vortex Gaussian Schell-model

vtvGSM vector twisted vortex Gaussian Schell-model

INTRODUCTION

In recent years, singular optics and the study of structured light has dramatically grown in significance and practicality. Structured light is light with non-trivial properties involving phase, coherence, polarization, angular momentum, etc. Singular optics encompasses studies of structured light with localized and extended singularities. These singularities encompasses a massive array of different optical phenomena. One of the most well known of these phenomena, and one that will be thoroughly used and explored throughout this dissertation, is known as an optical vortex. An optical vortex in a field is a singular point of zero intensity with a factor of 2π phase shift around that singularity. These vortices have found relevance in several optical applications including optical communications[1], coronagraphy [2], coherence filtering [3] laser detection and ranging systems[4], and optical tweezing[5], to name a few.

With their ever-growing prevalence in practical applications, it is valuable to explore the structure and use of optical vortices. One facet we are interested in is how to further control their structure and angular momentum. Beams that possess these optical vortices carry angular momentum that can be broken down into orbital angular momentum (OAM) and spin angular momentum (SAM). Orbital angular momentum is dependent on the spatial distribution of the field, thus it arises when there is a phase singularity. Spin angular momentum is dependent on the polarization handedness of the field. This angular momentum is what is employed in applications such as optical tweezing [5] and free space optical communications (FSOC)[6].

Another facet we explore is phenomena created through manipulating optical vortices. Due to their unique properties, optical vortices can be positioned such that they create a phenomena known as superoscillations [7, 8]. Superoscillations are oscillations of a wavefield that are locally higher than the bandlimit of the field. Bandlimiting is the limiting of a signal's spectral density to zero above a certain finite frequency. The local rate of oscillation of a real-valued signal can be characterized by

the separation of its zeros, with the space between two zeros representing one half of an oscillation. When the space is less than one half of a wavelength, the field in the region is said to be superoscillatory. It should be noted that moving said zeros does not change the bandlimit [9]. Optical vortices, being a point of zero intensity, can be used to represent this oscillation and thus create superoscillatory behavior. These superoscillations have been used to create lenses that produce subwavelength spots [10, 11, 12, 13, 14], thus they have gained practical interest.

We explore these characteristics and phenomena under partially coherent conditions. While there have been investigations into structured light with randomized field fluctuations, and there are classes of partially coherent beams that are used for optical communications, it is an area that demands further investigation. Partially coherent fields are of interest because they show promise in several practical areas from enhancing imaging [15], to laser collimation [16], to resisting turbulence along propagation [17]. It is through this dissertation that we explore several areas of partially coherent structured light to provide unique insight into the properties and behaviors of these phenomena.

Superoscillations have been largely studied under fully coherent conditions. This is partially because when randomizing the field fluctuations, the points of zero intensity often disappear [18, 19]. While this suggests that the superoscillatory behavior would break down, this is only true from the intensity perspective. Though coherent optical vortices dissipate as the coherence is decreased, analogous structures known as correlation vortices can appear in the correlation functions of partially coherent fields [20, 21]. This implies, and will be shown, that superoscillations must also appear in the correlation function of partially coherent fields. Considering the possibilities superoscillations bring to imaging and the array of applications for partially coherent fields, the exploration of the combination of these two phenomena is an exciting prospect.

The backbone of the mathematics used in each chapter involves the correlation function of the partially coherent fields. The function we employ is the cross-spectral density. The cross-spectral density is a two-point correlation function at a singular frequency that represents the spatial correlations at said frequency [22]. We use this because it allows us to study the average properties of the field and, as discussed previously, some optical phenomena can only be observed in the phase of the correlation function when the field is randomized.

In the first paper, we study superoscillations in partially coherent light using a number of models of partially coherent beams possessing vortex structures. To create these randomized fields, we use what is known as the beam wander model [23]. In this model, the axis of propagation of a paraxial beam is treated as a random function of transverse position. This allows us to control the coherence of the beam through a wander parameter. The lower the value of the wander parameter, the more coherent the beam becomes, being fully coherent when it is the smallest parameter in our model. We also create superoscillatory behavior in our modal coherence model. It consists of two closely spaced vortices modulated by a Gaussian envelope. We are able to treat this field as coherent superposition of Laguerre-Gauss (LG) beams which in turn lets us explore the effects of reducing the spatial coherence between the beams. It is with these models and variations of them that we show that it is possible in some cases for a decrease in coherence to decrease the spacing of superoscillatory zeros, thus increasing the superoscillatory behavior.

Our second paper extends this study of partially coherent superoscillations and explores a way to propagate these phenomena utilizing the Talbot effect. The Talbot effect is often described as the "self-imaging" of a diffraction grating. At fixed distances from the grating, referred to as the Talbot distance, the diffracted light forms an image of the grating itself. The Talbot effect has been used to study the stability of superoscillations on propagation when the source illuminating the Talbot grating is

a superoscillatory function [24]. We use the paraxial form of the Talbot effect and investigate how superoscillations of the Talbot grating manifest in the correlation function of the Talbot images as well as how the superoscillatory behavior reacts to changes in coherence. The superoscillatory function illuminating the grating creates a group of closely spaced zeros directly after the grating. These can be observed in the phase of the correlation function. Utilizing the Talbot effect, these superoscillations are reproduced at the primary and secondary Talbot images. The zeros of the cross-spectral density move closer together eventually annihilating as the spatial coherence is decreased. When the annihilation occurs, the superoscillatory behavior disappears. We show that changes in both the spatial coherence and the observation point can dramatically affect the superoscillatory behavior at the Talbot distance, therefore providing flexibility in tailoring these superoscillations for applications. All of the superoscillatory behavior work has been explored with an eye towards using partially coherent superoscillations in imaging applications such as superoscillatory lenses and super-resolution imaging [25].

Our third paper explores modification of the properties of partially coherent vortex beams in which our previous work utilizes. We are interested in the partially coherent class of vortex beams as they have shown to be resistant to turbulent fluctuations [1, 26], thus could be used to solve coupling issues that occur in free space optical communication [6]. We specifically focus on the twisted vortex Gaussian Schell-model beam (tvGSM) which can be constructed through the combination of a Rankine vortex beam and a twisted Gaussian Schell-model beam (tGSM) utilizing a superposition model. It has been shown that one can finely control the OAM of a tvGSM beam. We now incorporate polarization as an additional parameter alongside the vortex order and twist parameter to define a vector tvGSM (vtvGSM) beam [27]. This enables investigation of the control one can have over the SAM and total angular momentum in addition to the OAM. We show that with the addition of polarization there

is unprecedented control over the total angular momentum of the partially coherent beam. This control enables the creation of a counter-rotating beam. This is a beam in which the OAM and SAM rotate in opposite directions at the core and outskirts of the beam, enabling a positive angular momentum core surrounded by a negative angular momentum edge and visa versa. In addition, this control allows for a "dead zone" of angular momentum to be created in the core of the beam. The control and capabilities exhibited by the vtvGSM beam are useful in applications where the precise manipulation of angular momentum is a necessity, such as optical tweezing or free space optical communications.

CHAPTER 1: Superoscillatory Behavior in Partially Coherent Fields

ABSTRACT

Superoscillations are oscillations of a wavefield that are locally higher than the bandlimit of the field. Superoscillations have to date been studied primarily in coherent wavefields; here we look at superoscillations that appear in the phase of the correlation function in partially coherent fields. It is shown that a decrease in spatial coherence can in some cases strengthen the superoscillatory behavior, and in others decrease it. Superoscillations are studied in a number of model partially coherent fields, and the influence of coherence on each model is considered.

1.1 Introduction

It is now widely recognized that band-limited signals can possess regions where the local frequency is arbitrarily larger than the fastest oscillating Fourier component in the function. The oscillations in these regions are known as *superoscillations* [1,2]. The local rate of oscillation of a real-valued signal is often dictated by the separation of its zeros, with the space between two zeros representing one half of an oscillation; when the space is less than one half of a wavelength, the field in the region is said to be superoscillatory.

Superoscillations have been demonstrated by a number of mathematical techniques, but perhaps the simplest of these was done by Chremmos and Fikioris [3], who showed that zeros can be moved arbitrarily close together in a bandlimited function without any effect on the bandlimit; a similar construction was used to design superoscillations in the cross-section of a complex monochromatic optical field [4]. In such complex fields, superoscillations may be directly connected to the presence of optical vortices,

lines in three-dimensional space around which the field has a circulating or helical structure [5]. The creation of superoscillations may therefore be viewed as the control and manipulation of optical vortices and other field singularities.

As the superoscillatory zeros are moved closer together, the amplitude of the oscillations between them decreases. Furthermore, the superoscillatory region is inevitably surrounded by regions where the amplitude is significantly larger, becoming orders of magnitude larger even for modest gains in local frequency. Though at first glance this would appear to make superoscillations impractical, a number of researchers have designed and tested superoscillation-based lenses that can improve the resolution of imaging systems through the creation of subwavelength spots [6,7,8,9,10]. Superoscillations have therefore become of practical as well as scientific interest.

When a field possesses fluctuations in space and time, i.e. it is partially coherent, zeros of intensity typically disappear [11]. This in turn suggests that the superoscillatory behavior breaks down, as has been demonstrated in several studies [12,13]. Though coherent optical vortices disappear as the coherence is decreased, analogous structures can appear in the correlation functions of partially coherent fields. These *correlation vortices* or *coherence vortices* appear in the phase of a two-point correlation function when one observation point is fixed [14,15]; it has also been recognized that optical vortices evolve into correlation vortices as the spatial coherence of a vortex beam is decreased [16].

With these observations in mind, it is clear that superoscillations must also appear in partially coherent fields and, considering the numerous applications of partially coherent fields [17], it is natural to wonder whether superoscillations in correlation functions can also be applied to optical problems. In this paper, we study superoscillations in partially coherent light using a number of models of partially coherent beams possessing vortex structures. We begin by considering the randomization of a coherent beam possessing superoscillations, and are led to other possibilities. The

dependence of superoscillations on the correlation length of the source is studied, and we present some general remarks on the relationship between superoscillations and coherence.

1.2 Coherence theory and singularities

To characterize fields that possess random fluctuations, it is necessary to study the average properties of the field, in particular two-point correlation functions. Throughout this paper we will use the cross-spectral density, which can be defined as [18]

$$W(\mathbf{r}_1, \mathbf{r}_2, \omega) = \langle \tilde{U}(\mathbf{r}_1, \omega) U(\mathbf{r}_2, \omega) \rangle_\omega, \tag{1.1}$$

where $U(\mathbf{r}, \omega)$ represents a monochromatic scalar field and $\langle \cdots \rangle_\omega$ represents an average over an ensemble of monochromatic fields. For convenience, we use a tilde to represent the complex conjugate throughout the paper. The spectral density of the field, or intensity at frequency ω, can be found from the cross-spectral density with $\mathbf{r}_1 = \mathbf{r}_2 = \mathbf{r}$,

$$S(\mathbf{r}, \omega) = W(\mathbf{r}, \mathbf{r}, \omega). \tag{1.2}$$

One particularly important feature of the cross-spectral density is that it satisfies a pair of Helmholtz equations in the spatial variables $\mathbf{r}_1$ and $\mathbf{r}_2$,

$$\begin{aligned} \Delta_1^2 W(\mathbf{r}_1, \mathbf{r}_2, \omega) + k^2 W(\mathbf{r}_1, \mathbf{r}_2, \omega) = 0, \\ \Delta_2^2 W(\mathbf{r}_1, \mathbf{r}_2, \omega) + k^2 W(\mathbf{r}_1, \mathbf{r}_2, \omega) = 0, \end{aligned} \tag{1.3}$$

where Δ_1 represents the Laplacian with respect to $\mathbf{r}_1$, and so forth. When $\mathbf{r}_1$ is held fixed, the cross-spectral density will propagate like a monochromatic wave with respect to $\mathbf{r}_2$. As we know that optical vortices are common within monochromatic fields, the cross-spectral density with one position vector fixed should manifest vortices as well, which are referred to as correlation vortices. These vortices are generic

features for the cross spectral density.

We will be displaying and referring to vortex structures throughout the body of this paper. A vortex, in a field or a correlation function, can be identified as a point where all phase values converge. Though we have qualitatively described the structure of an optical vortex, it is convenient to provide a visual example as well. Figure 1.1 displays the intensity and the phase in the cross-section of a Laguerre-Gauss beam of radial order $n = 0$ and azimuthal order $m = 1$ in the waist plane of the beam; Laguerre-Gauss beams of non-zero azimuthal order possess a zero line on their propagation axis and possess a vortex structure around that axis. It can be clearly seen that the phase increases by 2π as one follows a counterclockwise path around the vortex core. For a correlation function, the phase represents the absolute position of fringes as measured in a wavefront splitting interferometer such as Young's interferometer.

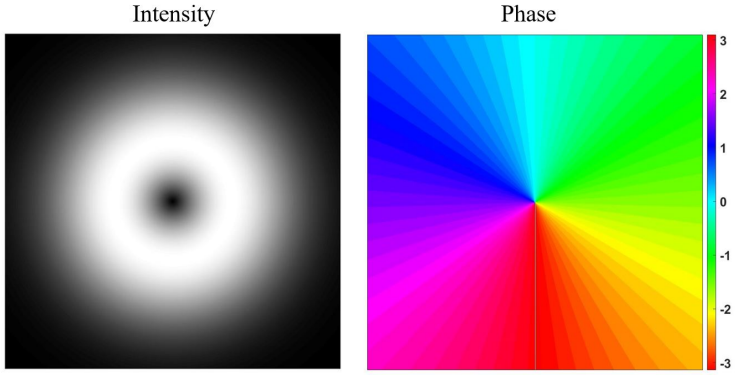

Figure 1.1: The intensity and Phase of a first order vortex within a Laguerre-Gauss beam of radial order $n = 0$ and azimuthal order $m = 1$.

It is to be noted that the strength of superoscillations is often characterized by a local wavenumber [19], which for the cross-spectral density is defined by the expression,

$$k(\mathbf{r}_1, \mathbf{r}_2) = \left| Im \frac{\nabla_{\mathbf{r}_2} W(\mathbf{r}_1, \mathbf{r}_2)}{W(\mathbf{r}_1, \mathbf{r}_2)} \right|. \tag{1.4}$$

This quantity measures rapid oscillations of the complex phase of a wavefield; however, the models we will introduce typically produce close-packed zeros, with a constant

phase between them, and the local wavenumber is not optimal for characterizing the behavior. Throughout this paper we monitor the superoscillatory behavior through measuring the separation distance between the singularities.

1.3 Partially coherent superoscillations

We are interested in exploring how altering the spatial coherence of a field affects any superoscillatory behavior contained in the field. We take the natural first step of setting up a coherent field that already contains superoscillations and study how this behavior changes as the spatial coherence is decreased.

We model a randomized superoscillatory field using what is known as the beam wander model [11]. In this model, the axis of propagation of a paraxial beam is treated as a random function of transverse position. The cross spectral density of such a field may be written as

$$W(\mathbf{r}_1, \mathbf{r}_2) = \int \tilde{U}(\mathbf{r}_1 - \mathbf{r}_0) U(\mathbf{r}_2 - \mathbf{r}_0) f(\mathbf{r}_0) d^2\mathbf{r}_0, \tag{1.5}$$

with $f(\mathbf{r}_0)$ being the probability density for the position of the axis and $\mathbf{r}_0$ being the transverse position on the axis, such that

$$f(\mathbf{r}_0) = \frac{1}{\pi\delta^2} \exp\left[-\frac{(x_0^2 + y_0^2)}{\delta^2}\right], \tag{1.6}$$

with $|\mathbf{r}_0|^2 = x_0^2 + y_0^2$ and δ represents the wander radius of the axis.

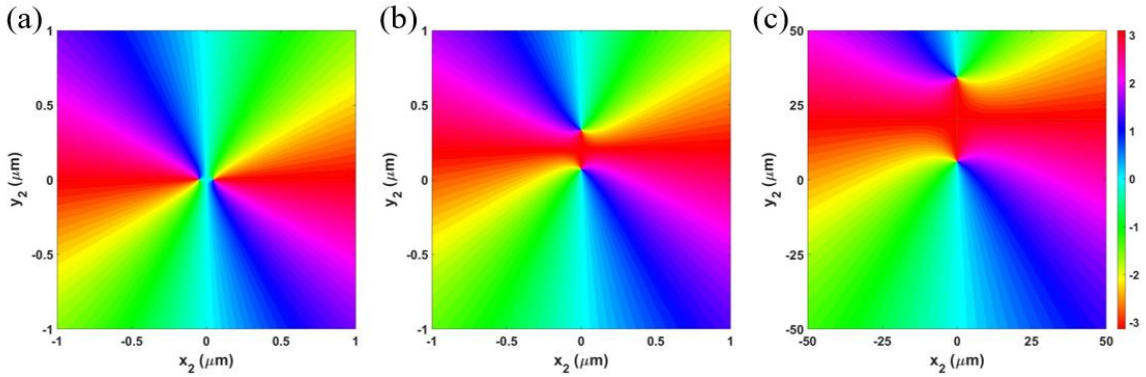

Figure 1.2: Phase of the cross-spectral density of two closely spaced vortices using the beam wander model. For each of the images above, $\lambda = 500nm$, $(x_1, y_1) = (0.0, 1000)\mu m$, $\sigma = 5mm$, and $\Delta = 0.1\lambda$. The wander radius δ and corresponding vortex separation distance α are (a) $\delta = 1\mu m$ and $\alpha = 0.1\mu m$, (b) $\delta = 10\mu m$ and $\alpha = 0.27\mu m$, (c) $\delta = 100\mu m$ and $\alpha = 28.3\mu m$. The plot range in (c) is increased to accommodate the very large vortex separation.

To study a partially coherent field possessing superoscillations, we choose for $U(\mathbf{r})$ the form,

$$U(\mathbf{r}) = (z + \Delta)(z - \Delta) \exp\left[-\frac{r^2}{2\sigma^2}\right], \tag{1.7}$$

where $z = x + iy$, σ is the beam width, and Δ is the complex spacing of the pair of vortices built into the function. In this model, δ is inversely related to the field coherence: a smaller delta corresponds to a more coherent field. We use a Gaussian beam for mathematical convenience; however, it is to be noted that a Gaussian function is not strictly bandlimited. Within the context of the paraxial approximation, a choice of Δ smaller than one quarter of the wavelength (with less than one half of a wavelength between the zeros) will accurately approximate superoscillatory behavior. The relationship between such "leaky" functions and superoscillations has been explored in depth elsewhere [20].

The integral of Eq. (1.5) is evaluated in Appendix A. The final result for the cross-

spectral density may be written as

$$W(\mathbf{r}_1, \mathbf{r}_2) = Q_1 \left[\frac{1}{A^3} + \frac{2\tilde{C}_1 C_2}{A^2} + \frac{\tilde{D}_1 D_2}{2A} \right], \tag{1.8}$$

where:

$$A = \frac{1}{\sigma^2} + \frac{1}{\delta^2}, \tag{1.9}$$

$$\tilde{D}_1 = \tilde{C}_1^2 - \Delta^2, \quad D_2 = C_2^2 - \Delta^2, \tag{1.10}$$

$$C_i = C_{ix} + iC_{iy}, \tag{1.11}$$

$$\begin{aligned} C_{1x} &= x_1 - \frac{\frac{x_1}{\tilde{\sigma}^2} + \frac{x_2}{\sigma^2}}{2A}, \quad C_{2x} = x_2 - \frac{\frac{x_1}{\tilde{\sigma}^2} + \frac{x_2}{\sigma^2}}{2A}, \\ C_{1y} &= y_1 - \frac{\frac{y_1}{\tilde{\sigma}^2} + \frac{y_2}{\sigma^2}}{2A}, \quad C_{2y} = y_2 - \frac{\frac{y_1}{\tilde{\sigma}^2} + \frac{y_2}{\sigma^2}}{2A}. \end{aligned} \tag{1.12}$$

The constant Q_1 is defined in Eq. (1.38). It is a combination of Gaussian functions which possess no zeros, and can be neglected in the study of superoscillations.

We now consider how the position of the superoscillatory vortex pair changes as the spatial coherence of the field is decreased. We study the vortex structure of the correlation function by holding position vector $\mathbf{r}_1$ fixed and evaluating the phase of the cross-spectral density with respect to $\mathbf{r}_2$. This phase is plotted in Fig. 1.2 for several values of δ, starting with the vortices separated by 0.1λ. As the coherence is decreased, the separation distance between the two vortices increases, reaching a half-wavelength separation when the wander radius approaches $10\mu m$. Furthermore, the vortices transition to being aligned along the y-axis instead of the x-axis, in line with the reference point. As can be seen in Fig. 1.2(c), the distance between vortices continues to increase as the wander radius increases.

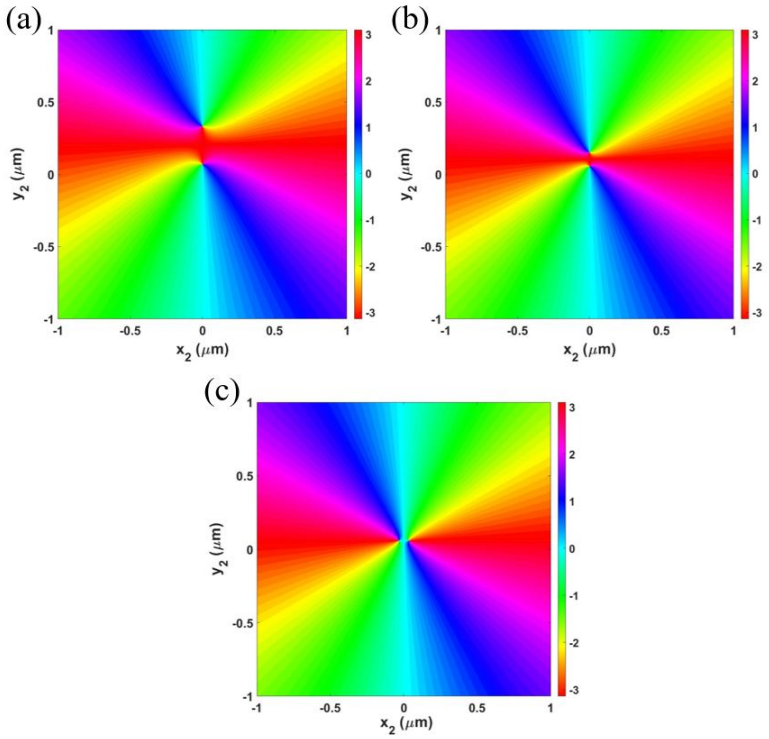

Figure 1.3: Phase of the cross-spectral density of two closely spaced vortices using the beam wander model. For each of the images above, $\lambda = 500nm$, $\delta = 10\mu m$, $\sigma = 5mm$, and $\Delta = .1\lambda$. The reference point position and corresponding vortex separation distance α are (a) $(x_1, y_1) = (0.0, 1000)\mu m$ and $\alpha = 0.27\mu m$, (b) $(x_1, y_1) = (0.0, 2000)\mu m$and $\alpha = 0.105\mu m$, (c) $(x_1, y_1) = (0.0, 4000)\mu m$ and $\alpha = 0.07\mu m$.

Qualitatively similar behavior arises when the reference point $\mathbf{r}_1$ is moved to other locations at a comparable radial distance from the beam axis, though the orientation of the vortices changes. For example, if the reference point is rotated to the x-axis, the vortices still separate as the spatial coherence is decreased, but they align along the x-axis, again in line with the reference point.

Though the preceding example indicates that the superoscillatory behavior is degraded as spatial coherence is decreased, it can be at least partly recovered if the reference point is moved significantly beyond the wander radius. Figure 1.3 shows the change in the vortex position as $\mathbf{r}_1$ is moved further from the axis. It can be seen that the correlation vortices, which had separated and moved to a vertical line, move back together along a horizontal line with increasing $|\mathbf{r}_1|$, looking very much like the

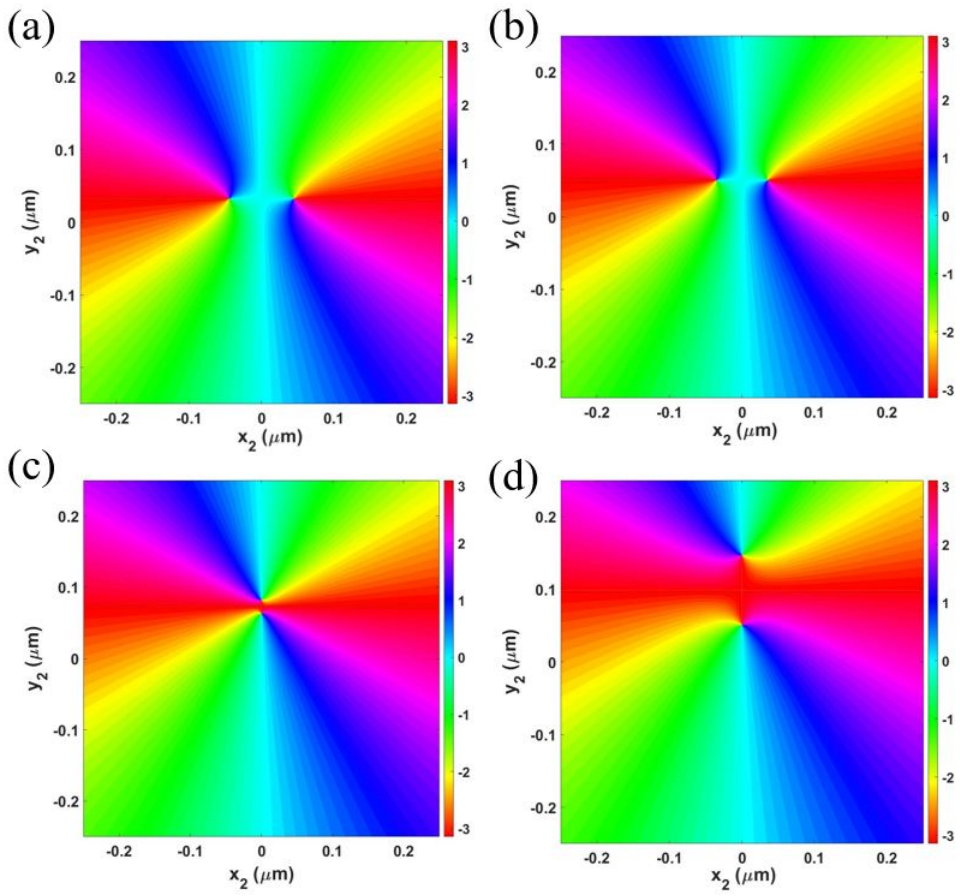

Figure 1.4: Phase of the cross-spectral density of two closely spaced vortices as the spatial coherence is incrementally lowered. For each of the images above, $\lambda = 500nm$, $(x_1, y_1) = (0.0, 1000)\mu m$, $\sigma = 5mm$, and $\Delta = 0.1\lambda$. The wander radius δ and corresponding vortex separation distance α are (a) $\delta = 4\mu m$ and $\alpha = 0.089\mu m$, (b) $\delta = 5\mu m$ and $\alpha = 0.071\mu m$, (c) $\delta = 6\mu m$ and $\alpha = 0.019\mu m$, and d) $\delta = 7\mu m$ and $\alpha = .096\mu m$.

decrease of spatial coherence has been reversed by moving the observation point.

We may interpret this effect as follows. The overall structure of the correlation function depends on the random fluctuations at both $\mathbf{r}_1$ and $\mathbf{r}_2$, and the correlations between them. As we move $\mathbf{r}_1$ outside the wander radius, the fluctuations of the field at this point are greatly reduced, resulting in the overall field appearing more coherent. This observation indicates that, with an appropriate choice of observation point, we may maintain the superoscillatory behavior of the field even as the spatial coherence decreases. It is to be noted that the position of $\mathbf{r}_1$ still lies within the beam

radius of $\sigma = 5mm$, so the field intensity at this point is still appreciable.

In both Figs. 1.2 and 1.3, the vortices change their orientation with respect to the origin. It is natural to ask how the separation distance of the vortices evolves as this transition occurs, and this is illustrated for a change of δ in Fig. 1.4. As we incrementally increase the wander radius, the singularities in fact come closer together at first, meaning that a decrease in partial coherence has enhanced the superoscillatory behavior. The singularities reach a minimum non-zero separation before moving along the vertical axis. It is to be noted that this enhancement occurs only for a small range of wander radii δ; however, this shows that the randomization of a field, under the right circumstances, can decrease the separation distance between two singularities.

1.4 Partially coherent superoscillations from higher-order vortex beams

The first example above indicates that, outside of small range of δ values, a decrease in spatial coherence tends to increase the spacing between correlation vortices in a wavefield. We may use this observation, however, as a strategy to produce superoscillations in a partially coherent field from a higher-order vortex beam. It is well-known that higher-order vortices are unstable, non-generic, features of a wavefield that will break into a collection of first-order vortices under wavefield perturbations. Such perturbations include a decrease in spatial coherence, as has been shown in Ref. [21]. Thus we can make a superoscilatory partially coherent field by perturbing a higher-order vortex beam, as we illustrate next.

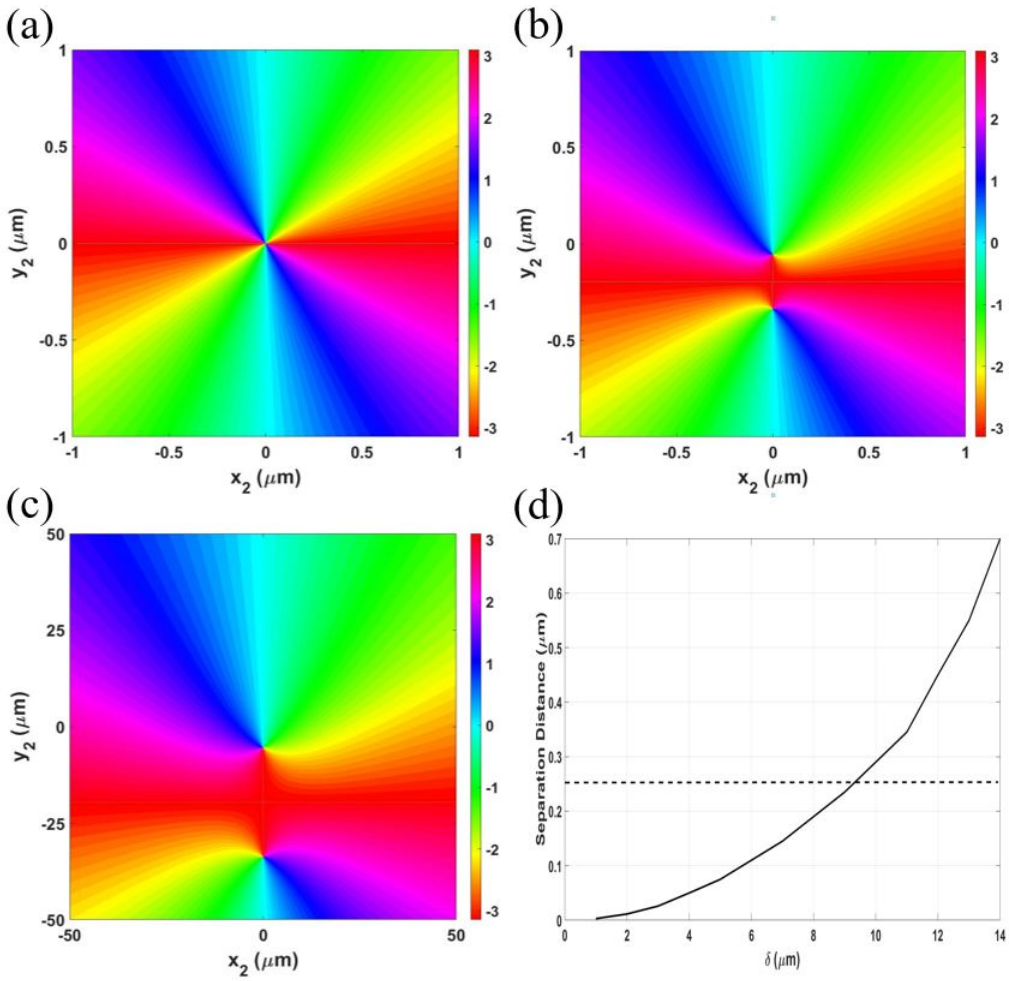

Figure 1.5: Phase of the cross-spectral density of a second order vortex and its subsequent first order vortices. For each of the images above, $\lambda = 500nm$, $(x_1, y_1) = (0.0, 1000)\mu m$, $\sigma = 5mm$. In the figure: (a) $\delta = 1\mu m$, (b) $\delta = 10\mu m$, (c) $\delta = 100\mu m$. (d) shows the relationship between the increase in wander radius (decrease in coherence), and the separation distance between the two singularities.

We consider the randomization of a second-order Laguerre-Gauss beam, of order $n = 0$, $m = 2$, of the form

$$U_{0,2}^{LG}(x, y) = \sqrt{\frac{2}{2\pi\sigma^2}} \left(\frac{\sqrt{2}}{\sigma}\right)^2 (x \pm iy)^2 \exp\left[-\frac{1}{\sigma^2}(x^2 + y^2)\right], \tag{1.13}$$

where σ is the beam width at the waist plane $z = 0$. We use this beam in Eq. (1.5) to generate the cross-spectral density, which is a special case of the class of beams

given in [22]. The cross-spectral density may be written as

$$W(\mathbf{r}_1,\mathbf{r}_2)=\pi F(\mathbf{r}_1,\mathbf{r}_2)\Bigg\{\sum_{l=0}^{1}\binom{2}{l}^2\frac{\Gamma(l+1)}{A^{4-l+1}}\left[\frac{1}{\alpha^2}(x_2\pm iy_2)-\frac{1}{\sigma^2}(x_1\pm iy_1)\right]^{2-l} \times\left[\frac{1}{\alpha^2}(x_1\mp iy_1)-\frac{1}{\sigma^2}(x_2\mp iy_2)\right]^{2-l}+\frac{\Gamma(3)}{A^3}\Bigg\}, \tag{1.14}$$

where A is the same as in Eq. (1.9), and

$$\frac{1}{\alpha^2}\equiv\left[\frac{1}{\sigma^2}+\frac{1}{\delta^2}\right]. \tag{1.15}$$

The quantity $F(\mathbf{r}_1,\mathbf{r}_2)$ represents the envelope of a Gaussian Schell-model beam as defined by

$$F(\mathbf{r}_1,\mathbf{r}_2)\equiv\frac{|C|^2}{\pi\delta^2}\exp\left[-\frac{r_1^2}{A\delta^2\tilde{\sigma}^2}\right]\exp\left[-\frac{r_2^2}{A\delta^2\sigma^2}\right]\exp\left[-\frac{|\mathbf{r}_1-\mathbf{r}_2|^2}{A|\sigma|^4}\right]. \tag{1.16}$$

Figure 1.5 shows the phase of the cross-spectral density as a function of δ. In the coherent limit, the phase of the cross-spectral density manifests a single second-order vortex at the origin. As the coherence decreases, the second-order vortex separates into 2 first-order singularities that are very close together, exhibiting superoscillatory behavior. As with the previous example, as the coherence is further decreased, the vortices will separate enough that they no longer represent superoscillations.

One particular point of interest is to look at the rate at which the two first-order singularities separate while still being superoscillatory. Figure 1.5(d) shows the the relationship between the wander radius and the separation distance between the singularities. It is immediately apparent that it only requires a small decrease in coherence, with a wander radius much smaller than the beam width, to increase the separation distance to the point that we would no longer consider the field to be superoscillatory. This limit is shown as the dotted line in Fig. 1.5(d), which represents a half-wavelength separation distance. We used a wander radius of $1\mu m$ to represent

the coherent limit. For a wander radius of $9\mu m$, the vortex separation increases to approximately 250 nm, equal to a half-wavelength.

This example shows we can create superoscillations in a partially coherent field by decreasing the spatial coherence of a second-order vortex beam. If we use an even higher-order vortex beam, we can get a line of correlation vortices representing an extended region of superoscillatory behavior. Again, a change in the position of the observation point allows one to change the orientation of the line of vortices.

Here we have explicitly used the observation that a decrease of coherence in the beam wander model results in a decrease in superoscillatory behavior. This brings us to wonder if there are any scenarios in which a decrease in coherence can bring about an increase in superoscillatory behavior. This is explored in the next section.

1.5 Modal coherence model

The previous examples showed that superoscillatory behavior tends to decrease as the spatial coherence of a field is significantly lowered. However, this is not a universal behavior. It is possible to introduce fields for which the zero spacing decreases as the coherence is decreased, as we now show.

We again consider a field of two closely-spaced vortices modulated by a Gaussian envelope, as in Eq. (1.7). Again, Δ is the separation of the vortices, σ is the width of the Gaussian, and $z = x + iy$. The zeros are aligned along the y-axis for this case, so that Δ is pure imaginary.

We now rewrite Eq. (1.7) as a coherent superposition of Laguerre-Gauss (LG) beams of orders (0,0) and (0,2). The field then takes the form,

$$U(\mathbf{r}) = U_{02}(\mathbf{r}) - \Delta^2 U_{00}(\mathbf{r}) \tag{1.17}$$

where

$$U_{02}(\mathbf{r}) = z^2 \exp\left[-\frac{r^2}{2\sigma^2}\right], \tag{1.18}$$

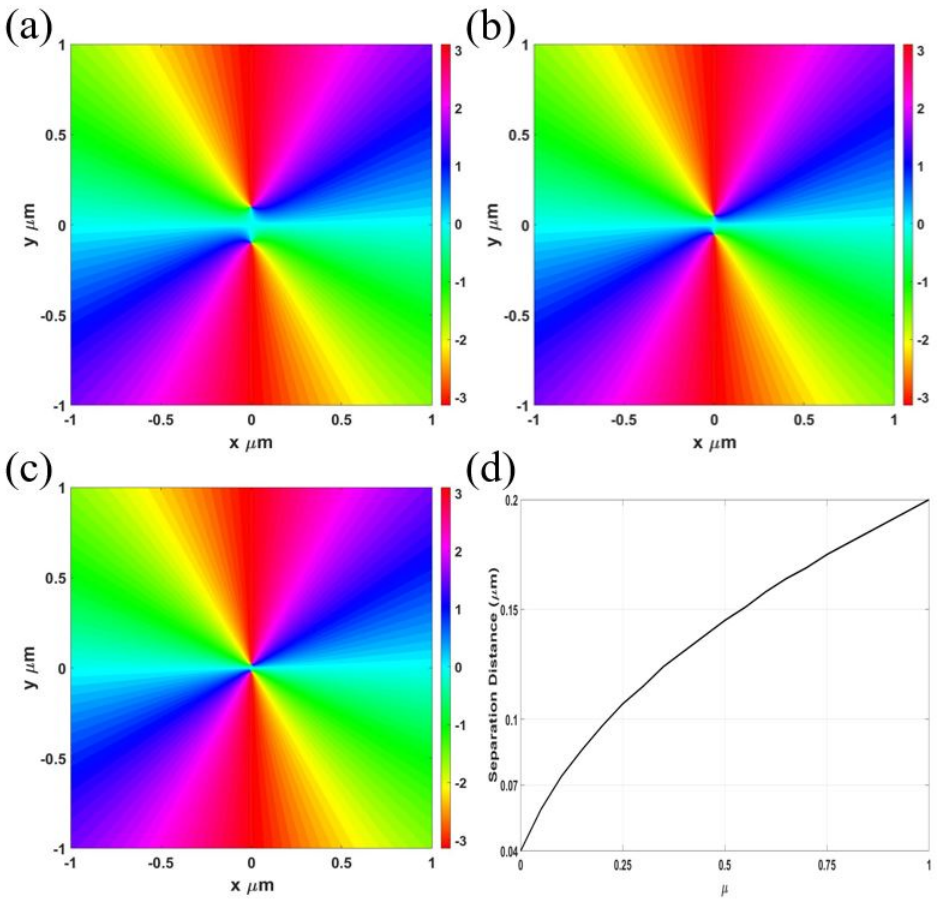

Figure 1.6: Phase of the cross-spectral density of two closely spaced vortices as a function of $\mathbf{r}_2$ with $\mathbf{r}_1 = (0.5, 0)$. Here $\Delta = 0.1i\mu m$ and $\sigma = 1\mu m$. The degree of coherence and the corresponding separation distance α for the first three figures are (a) $\mu = 1$ and $\alpha = 0.2\mu m$,(b) $\mu = 0.25$ and $\alpha = 0.1\mu m$, (c) $\mu = 0$ and $\alpha = 0.02\mu m$. (d) shows the relationship between the change in degree of coherence and the separation distance between the singularities.

and

$$U_{00}(\mathbf{r}) = \exp\left[-\frac{r^2}{2\sigma^2}\right]. \tag{1.19}$$

We have left off the traditional normalization of the LG beams for simplicity. By treating our superoscillatory field as a superposition of LG beams, we can now explore the effect of reducing the spatial coherence between the beams. If we imagine that the overall coherence between the beams is characterized by the complex degree of coherence μ, we can find the cross-spectral density by taking the product of $\tilde{U}(\mathbf{r}_1)$

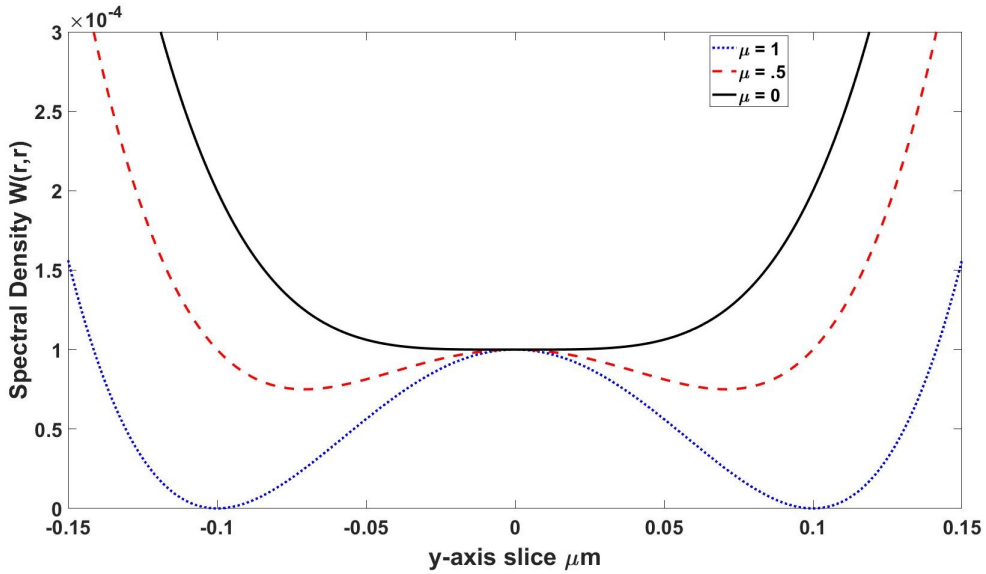

Figure 1.7: The spectral density S($\mathbf{r}$,ω) along the y-axis of two closely spaced vortices as a function of $\mathbf{r}_2 = \mathbf{r}_1 = \mathbf{r}$. Here $\Delta = 0.1i\mu m$ and $\sigma = 1\mu m$.

with $U(\mathbf{r}_2)$, and introducing the factor μ into the cross terms, giving the result,

$$W(\mathbf{r}_1, \mathbf{r}_2) = \exp\left[-\frac{r_1^2}{2\sigma^2}\right] \exp\left[-\frac{r_2^2}{2\sigma^2}\right] \left[\tilde{z}_1^2 z_2^2 - \tilde{\mu}\Delta^2 \tilde{z}_1^2 - \mu\tilde{\Delta}^2 z_2^2 + \tilde{\Delta}^2\Delta^2\right]. \quad (1.20)$$

Figure 1.6 shows the phase of the cross-spectral density for decreasing values of μ, taken to be real for simplicity. The vortices, which are already superoscillatory for $\mu = 1$, move closer together as the degree of coherence is decreased: the superoscillatory behavior becomes stronger. Figure 1.6(d) shows that the zero spacing is $0.08\mu m$ for $\mu = 0$, one sixth of a wavelength. This example demonstrates that a decrease of coherence can, under the right circumstances, create or strengthen superoscillations.

There is one significant advantage to be found in using partially coherent fields to produce superoscillations. Figure 1.7 displays the spectral density (intensity) of the field, as defined in Eq. (1.2), along the y-axis as the degree of coherence is lowered. The zeros of intensity for the fully coherent field disappear as the spatial coherence is decreased, resulting in a uniform low, but non-zero, intensity in the region of the correlation vortices. Because correlation vortices do not have to appear at regions

of zero intensity, it is possible to have appreciable light in a superoscillatory region, a strong difference from the coherent case. Though the intensity is still low for this example, more sophisticated examples might demonstrate superoscillatory correlation functions in regions of high intensity.

We noted earlier that we have been using beams which are only approximately bandlimited, i.e. "leaky." The modal model for a partially coherent superoscillatory beam presented here, however, is simple enough to be adapted to a true bandlimited field using Bessel beams. Noting that, for a small argument, a Bessel beam may be approximated by the form,

$$J_n(x) \approx \frac{1}{n!}\left(\frac{x}{2}\right)^n, \tag{1.21}$$

we may construct a coherent field with zeros approximately at positions $\pm\Delta$ using the expression,

$$U(\mathbf{r}) = -\Delta^2 J_0(\gamma r) + \frac{8}{\alpha^2} J_2(\gamma r) e^{2i\phi}, \tag{1.22}$$

where γ may be identified as the inverse width of the Bessel beam. By assuming a degree of coherence μ between the zeroth and second order Bessel components of the field, we can again study how the superoscillations change as μ is decreased. We again chose $\mathbf{r}_1 = (0.5, 0)$, $\Delta = 0.1i\mu m$, and $\lambda = 500nm$ as in Fig. 1.6. The quantity $\gamma = 5\mu m$, which corresponds to a Bessel beam with an opening angle of 23°. The evolution of the vortices of the correlation function matched the results of Fig. 1.6 almost exactly, showing that we get the same superoscillatory behavior for a true bandlimited function.

1.6 Modal coherence: Radial Case

For imaging applications, a superoscillatory spot created with a zero ring is preferable to a superoscillation created with a pair of point zeros. In 2020, for example, Smith and Gbur [10] demonstrated how to generalize the method of Chremmos and Fikioris [3] to produce a superoscillatory point-spread function using ring zeros. Here,

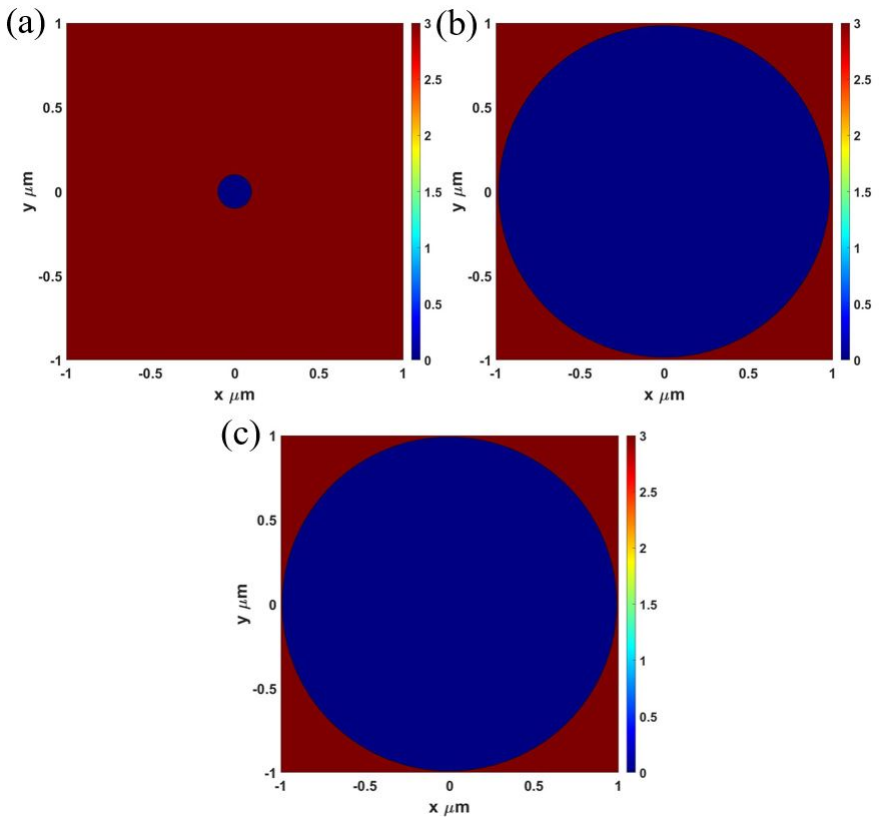

Figure 1.8: Phase of the cross-spectral density of the radial mode of the example demonstrated in figure 3. : in this case $r_0 = 0.1\mu m$, $\sigma = 0.5\mu m$, and $(x_1, y_1 = (0.05, 0.0)$. In the figure, (a) $\mu = 1$,(b) $\mu = 0.5$,(c) $\mu = 0$.

we explore whether the modal coherence method of the previous section can be used to produce superoscillatory spots in the cross-spectral density.

We now work with LG modes of different radial order, which possess zero rings, instead of modes of different azimuthal order. We alter Eqns. (1.17), (1.18), and (1.19) to instead produce a zero ring at a radial position r_0. We have

$$\begin{aligned} U(r) &= \frac{r_0^2 - r^2}{2\sigma^2} \exp\left[-\frac{r^2}{2\sigma^2}\right] \\ &= U_{10}(r) - \left(1 - \frac{r_0^2}{2\sigma^2}\right) U_{00}(r), \end{aligned} \tag{1.23}$$

$$U_{10}(r) = \left(1 - \frac{r^2}{2\sigma^2}\right) \exp\left[-\frac{r^2}{2\sigma^2}\right], \tag{1.24}$$

$$U_{00}(r) = \exp\left[-\frac{r^2}{2\sigma^2}\right]. \tag{1.25}$$

Taking these adjustments into account and utilizing the same process as the previous example. The cross-spectral density for the radial case can be show to be:

$$\begin{aligned} W(\mathbf{r}_1, \mathbf{r}_2) = \exp\left[-\frac{r_1^2}{2\sigma^2}\right] \exp\left[-\frac{r_2^2}{2\sigma^2}\right] \Bigg[\left(1 - \frac{r_1^2}{2\sigma^2}\right) \\ \times \left(1 - \frac{r_2^2}{2\sigma^2}\right) - \tilde{\mu}\left(1 - \frac{r_0^2}{2\sigma^2}\right)\left(1 - \frac{r_1^2}{2\sigma^2}\right) \\ - \mu\left(1 - \frac{r_0^2}{2\sigma^2}\right)\left(1 - \frac{r_2^2}{2\sigma^2}\right) + \left(1 - \frac{r_0^2}{2\sigma^2}\right)^2\Bigg]. \end{aligned} \tag{1.26}$$

The radius of the zero ring can be determined the bracketed term of equation 1.26. If we set that term equal to zero and solve for r_2^2, we find the zero ring has a radius in r_2 given by

$$r_2^2 = 2\sigma^2\left[1 - \frac{\tilde{\mu}\left(1 - \frac{r_0^2}{2\sigma^2}\right)\left(1 - \frac{r_1^2}{2\sigma^2}\right) - \left(1 - \frac{r_0^2}{2\sigma^2}\right)^2}{\left(1 - \frac{r_1^2}{2\sigma^2}\right) - \mu\left(1 - \frac{r_0^2}{2\sigma^2}\right)}\right]. \tag{1.27}$$

This allows us to determine the spot size of this field for any values of r_1, r_0, and μ.

Figure 1.8 gives an example of the phase of the cross-spectral density as the coherence is decreased; the discontinuous jump represents the zero ring, across which the phase changes by π. We see that the size of the ring increases as the spatial coherence is decreased. It should be noted that the spot size rapidly expands to its limiting value, and thus the ring radii in (b) and (c) are almost identical. Though we used a modal method for introducing partial coherence, the result is similar to that of the beam wander model. The difference appears to arise due to the different functional forms of the modes in the radial ring case and the vortex case. It may be possible to produce rings that decrease in size as the coherence decreases, if more complicated combinations of modes are used.

1.7 Practical considerations

The model sources used in the aforementioned examples can doubtless be produced by a variety of methods, but it is worthwhile to give an example of how each can be generated, at least in principle.

A simple method for producing a beam satisfying the beam wander model is shown in Fig. 1.9(a), and was first described in [21]. A partially coherent illuminating field of Schell-model form, such as can be produced by passing light through a rotating ground glass plate, is passed through a vortex phase mask and then focused. The field in the focal plane will have the form of Eq. (1.5). Recently, it has been noted that partially coherent fields of the beam wander form possess unique topological characteristics on propagation [23]. To produce partially coherent superoscillatory fields, the simple vortex phase mask can be replaced by a mask producing the phase structure of Eq. (1.7).

The modal coherence model consists of a direct superposition of two Laguerre-Gauss modes of different orders with a global degree of coherence μ between them. Such a method could be produced, for example, by using a Mach-Zender interferometer, as shown in Fig. 1.9(b). In each arm of the interferometer, an SLM can be used as a mirror and to produce the desired mode. One mirror in one arm of the interferometer can be vibrated to produce a random phase fluctuation to produce partial coherence.

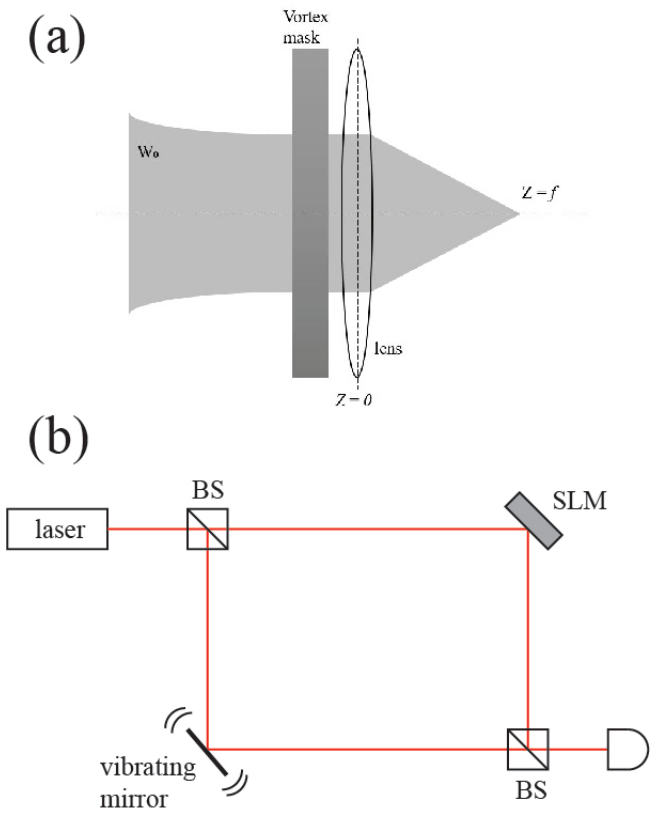

Figure 1.9: Simple experimental schemes for producing (a) the beam wander model, and (b) a partially coherent mode combination.

1.8 Concluding remarks

In this paper, we have explored the effect of partial coherence on superoscillatory behavior. Several different models were used to generate partial coherence, which have shown that it is possible in some cases for a decrease in coherence to decrease the spacing of superoscillatory zeros. The zeros manifest in the two-point cross-spectral density instead of the spectral density of the field, which means the rapid oscillations of the superoscillatory phase can be see even in locations where the light intensity is not close to zero. Sensing schemes which take advantage of interferometry to image objects and otherwise detect their structure could potentially benefit from such partially coherent superoscillations, and it is hoped that this work will stimulate further investigations into the physical and practical implications of these structures.

REFERENCES

[1] M. Berry, N. Zheludev, Y. Aharonov, F. Colombo, I. Sabadini, D.C. Struppa, J. Tollaksen, E.T.F. Rogers, F. Qin, M. Hong, X. Luo, R. Remez, A. Arie, J.B. Götte, M.R. Dennis, A.M.H. Wong, G.V. Eleftheriades, Y. Eliezer, A. Bahabad, G. Chen, Z. Wen, G. Liang, C. Hao, C-W Qiu, A. Kempf, E. Katzav, and M. Schwartz. Roadmap on superoscillations. *Journal of Optics*, 21(5):053002, apr 2019.

[2] G. Gbur. Using superoscillations for superresolved imaging and subwavelength focusing. *Nanophotonics*, 8(2):205-225, 01 Feb. 2019.

[3] I. Chremmos and G. Fikioris. Superoscillations with arbitrary polynomial shape. *Journal of Physics A: Mathematical and Theoretical*, 48(26):265204, jun 2015.

[4] M.K. Smith and G. Gbur. Construction of arbitrary vortex and superoscillatory fields. *Opt. Lett.*, 41(21):4979-4982, Nov 2016.

[5] G.J. Gbur. *Singular Optics*. CRC Press, 2017.

[6] A.M.H. Wong and G.V. Eleftheriades. Sub-wavelength focusing at the multi-wavelength range using superoscillations: an experimental demonstration. *IEEE Trans. Antenn. Propag.*, 59:4766-4776, 2011.

[7] E.T.F. Rogers, J. Lindberg, T. Roy, S. Savo, J.E. Chad, M.R. Dennis, and N.I. Zheludev. A super-oscillatory lens optical microscope for subwavelength imaging. *Nature Materials*, 11:432-435, 2012.

[8] E.T.F. Rogers, S. Savo, J. Lindberg, T. Roy, M.R. Dennis, and N.I. Zheludev. Superoscillatory optical needle. *Appl. Phys. Lett.*, 102:031-108, 2013.

[9] T. Roy, E.T.F. Rogers, G. Yuan, and N.I. Zheludev. Point spread function of the optical needle super-oscillatory lens. *Appl. Phys. Lett.*, 104:231109, 2014.

[10] M.K. Smith and G. Gbur. Mathematical method for designing superresolution lenses using superoscillations. *Opt. Lett.*, 45(7):1854-1857, Apr 2020.

[11] G.Gbur, T.D. Visser, and E. Wolf. hidden singularities in partially coherent wavefields. *Journal of Optics A: Pure and Applied Optics*, 6(5):S239-S242, apr 2004.

[12] M.V. Berry. Suppression of superoscillations by noise. *Journal of Physics A: Mathematical and Theoretical*, 50(2):025003, dec 2016.

[13] E. Katzav, E. Perlsman, and M. Schwartz. Yield statistics of interpolated superoscillations. *Journal of Physics A: Mathematical and Theoretical*, 50(2):025001, dec 2016.

[14] I.D. Maleev, D.M. Palacios, A.S. Marathay, and G.A. Swartzlander, Jr. Spatial correlation vortices in partially coherent light: theory. *J. Opt. Soc. Am. B*, 21:1895-1900, 2004.

[15] D.M. Palacios, I.D. Maleev, A.S. Marathay, , and Jr. G.A. Swartzlander. Spatial correlation singularity of a vortex field. *Phys. Rev. Lett.*, 92:143905, 2004.

[16] G. Gbur and T.D. Visser. Coherence vortices in partially coherent beams. *Opt. Commun.*, 222:117-125, 2003.

[17] O. Korotkova and G. Gbur. Chapter four - applications of optical coherence theory. In Taco D. Visser, editor, *A Tribute to Emil Wolf*, volume 65 of *Progress in Optics*, pages 43-104. Elsevier, 2020.

[18] L. Mandel and E. Wolf. *Optical Coherence and Quantum Optics*. Cambridge University Press, 1995.

[19] Mark R. Dennis, Alasdair C. Hamilton, and Johannes Courtial. Superoscillation in speckle patterns. *Opt. Lett.*, 33(24):2976-2978, Dec 2008.

[20] M.V. Berry. Superoscillations and leaky spectra. *Journal of Physics A: Mathematical and Theoretical*, 52:015-202, 2019.

[21] Y. Gu and G. Gbur. Topological reactions of optical correlation vortices. *Optics Communications*, 282(5):709-716, 2009.

[22] C.S.D. Stahl and G. Gbur. Partially coherent vortex beams of arbitrary order. *J. Opt. Soc. Am. A*, 34(10):1793-1799, Oct 2017.

[23] Y. Zhang, Y. Cai, and G. Gbur. Partially coherent vortex beams of arbitrary radial order and a van cittert-zernike theorem for vortices. *Phys. Rev. A*, 101:043812, Apr 2020.

APPENDIX: Cross-spectral Density of the Beam Wander Model

In this appendix, we will evaluate equation 1.5, showing the steps leading to the cross-spectral density presented in equation 1.8. We begin with a field of

$$U(r) = (z+\Delta)(z-\Delta)\exp\left[-\frac{r^2}{2\sigma^2}\right]. \tag{1.28}$$

In this field, σ is the beam width and Δ is the spacing of the zeros. The beam wander model is realized with a cross spectral density of

$$W(\mathbf{r}_1,\mathbf{r}_2) = \int \tilde{U}(\mathbf{r}_1-\mathbf{r}_0)U(\mathbf{r}_2-\mathbf{r}_0)f(\mathbf{r}_0)d^2\mathbf{r}_0. \tag{1.29}$$

$f(\mathbf{r}_0)$ is the probability density for the position of the axis and $\mathbf{r}_0$ is the transverse position on the axis. In this case, $f(\mathbf{r}_0)$ is

$$f(\mathbf{r}_0) = \frac{1}{\pi\delta^2}\exp\left[-\frac{(x_0^2+y_0^2)}{\delta^2}\right]. \tag{1.30}$$

δ is the wander radius, which is the coherence parameter for our model. The cross-spectral density for our field is thus initially defined as

$$\begin{aligned} W(\mathbf{r}_1,\mathbf{r}_2) = \frac{1}{\pi\delta^2}\int &(\tilde{z}_1-\tilde{z}_0+\Delta)(\tilde{z}_1-\tilde{z}_0-\Delta)(z_2-z_0+\Delta)(z_2-z_0-\Delta) \\ &\times\exp\left[-\frac{(\mathbf{r}_1-\mathbf{r}_0)^2}{2\sigma^2}\right]\exp\left[-\frac{(\mathbf{r}_2-\mathbf{r}_0)^2}{2\sigma^2}\right]\exp\left[-\frac{r_0^2}{\delta^2}\right]d^2r_0. \end{aligned} \tag{1.31}$$

We begin simplifying by grouping the $\mathbf{r}_0$ terms together, giving

$$\begin{aligned} W(\mathbf{r}_1,\mathbf{r}_2) = \frac{1}{\pi\delta^2}\int &\left[(\tilde{z}_1-\tilde{z}_0)^2-\Delta^2\right]\left[(z_2-z_0)^2-\Delta^2\right]\exp\left[-\frac{r_1^2}{2\sigma^2}\right]\exp\left[-\frac{r_2^2}{2\sigma^2}\right] \\ &\times\exp\left[\frac{(\mathbf{r}_1+\mathbf{r}_2)\cdot\mathbf{r}_0}{\sigma^2}\right]\exp\left[-\left(\frac{1}{\sigma^2}+\frac{1}{\delta^2}\right)r_0^2\right]d^2r_0. \end{aligned} \tag{1.32}$$

We introduce a new function Q, defined as

$$Q = \frac{1}{\pi\delta^2} \exp\left[-\frac{r_1^2}{2\sigma^2}\right] \exp\left[-\frac{r_2^2}{2\sigma^2}\right]. \tag{1.33}$$

In Cartesian coordinates, the cross-spectral density now has the form,

$$W(\mathbf{r}_1, \mathbf{r}_2) = Q \int \left[[(x_1 - x_0) - i(y_1 - y_0)]^2 - \Delta^2\right] \left[[(x_2 - x_0) + i(y_2 - y_0)]^2 - \Delta^2\right] \times \exp\left[\frac{(x_1 + x_2)x_0 + (y_1 + y_2)y_0}{\sigma^2}\right] \exp\left[-\left(\frac{1}{\sigma^2} + \frac{1}{\delta^2}\right) r_0^2\right] d^2 r_0. \tag{1.34}$$

Now we complete the square with respect to the x_0 and y_0 exponents with the introduction of the quantities:

$$A = \frac{1}{\sigma^2} + \frac{1}{\delta^2}, \tag{1.35}$$

$$B_x = \frac{x_1}{\tilde{\sigma}^2} + \frac{x_2}{\sigma^2}, \tag{1.36}$$

$$B_y = \frac{y_1}{\tilde{\sigma}^2} + \frac{y_2}{\sigma^2}, \tag{1.37}$$

and the definition of a new function

$$Q_1 = Q \exp\left[\frac{B_x^2}{4A}\right] \exp\left[\frac{B_y^2}{4A}\right]. \tag{1.38}$$

This process reduces the cross-spectral density to the form

$$W(\mathbf{r}_1, \mathbf{r}_2) = Q_1 \int \left[[(x_1 - x_0) - i(y_1 - y_0)]^2 - \Delta^2\right] \left[[(x_2 - x_0) + i(y_2 - y_0)]^2 - \Delta^2\right] \times \exp\left[-A\left(x_0 - \frac{B_x}{2A}\right)^2\right] \exp\left[-A\left(y_0 - \frac{B_y}{2A}\right)^2\right] d^2 r_0. \tag{1.39}$$

We now do the coordinate transformation,

$$X = x_0 - \frac{B_x}{2A}, \tag{1.40}$$

$$Y = y_0 - \frac{B_y}{2A}, \tag{1.41}$$

providing us with a cross-spectral density defined as

$$\begin{aligned} W(\mathbf{r}_1, \mathbf{r}_2) = Q_1 \int & \left[[(x_1 - X - \frac{B_x}{2A}) - i(y_1 - Y - \frac{B_y}{2A})]^2 - \Delta^2 \right] \\ & \times \left[[(x_2 - X - \frac{B_x}{2A}) + i(y_2 - Y - \frac{B_y}{2A})]^2 - \Delta^2 \right] \\ & \times \exp\left[-AX^2\right] \exp\left[-AY^2\right] dX dY. \end{aligned} \tag{1.42}$$

To evaluate the integrals, we define the terms

$$\begin{aligned} -C_{1x} = -x_1 + \frac{B_x}{2A}, -C_{2x} = -x_2 + \frac{B_x}{2A}, \\ -C_{1y} = -y_1 + \frac{B_y}{2A}, -C_{2y} = -y_2 + \frac{B_y}{2A}. \end{aligned} \tag{1.43}$$

We additionally define the following complex quantities,

$$C_i = C_{ix} + iC_{iy}, Z = X + iY, \tilde{Z} = X - iY. \tag{1.44}$$

Applying all of the above definitions, and plugging them into the cross-spectral density, we simplify our integral to the form,

$$W(\mathbf{r}_1, \mathbf{r}_2) = Q_1 \int e^{-A(X^2+Y^2)} \left[(\tilde{C}_1 + \tilde{Z})^2 - \Delta^2 \right] \left[(C_2 + Z)^2 - \Delta^2 \right] dX dY. \tag{1.45}$$

We introduce a final pair of constants,

$$\tilde{D}_1 = \tilde{C}_1^2 - \Delta^2, D_2 = C_2^2 - \Delta^2. \tag{1.46}$$

All components of the integrand are now in powers of Z and $\tilde{Z}$. By converting to polar coordinates, we find that a number of components of the integral evaluate to zero, and we are left with

$$W(\mathbf{r}_1, \mathbf{r}_2) = Q_1 \int \left[r^4 + 4\tilde{C}_1 C_2 r^2 + \tilde{D}_1 D_2 \right] r dr d\phi. \tag{1.47}$$

This integral can be readily solved, allowing us to write our final expression for the cross-spectral density as

$$W(\mathbf{r}_1, \mathbf{r}_2) = Q_1 \left[\frac{1}{A^3} + \frac{2\tilde{C}_1 C_2}{A^2} + \frac{\tilde{D}_1 D_2}{2A} \right]. \tag{1.48}$$

CHAPTER 2: Partially coherent superoscillations in the Talbot effect

ABSTRACT

Oscillations of a wavefield that are locally higher than the bandlimit of the field are known as superoscillations. Superoscillations have to date been studied primarily in coherent wavefields; here we look at superoscillations that appear in the phase of the correlation function in partially coherent Talbot carpets. Utilizing the Talbot effect, it is shown that superoscillations can be propagated into the far field, even under a decrease in spatial coherence. It is also shown that this decrease in spatial coherence can strengthen the superoscillatory behavior at the primary and secondary Talbot images.

2.1 Introduction

It is now widely recognized that band-limited signals can possess regions where the local frequency is arbitrarily larger than the fastest oscillating Fourier component in the function. The oscillations in these regions are known as superoscillations [1,2,3]. Superoscillations have been rigorously mathematically discussed with their relation to quantum mechanics and the Schrödinger equation in [4]. In a real-valued spatial wavefunction, the local rate of oscillation is dictated by the separation of its zeros, with the space between two zeros representing one half of an oscillation; when the space is less than one half of a wavelength, the field in the region is said to be superoscillatory. Superoscillations of this type can be constructed by a variety of mathematical techniques, but the simplest of these is through the direct placement of polynomial zeros in a one-dimensional [5] or two-dimensional [6] bandlimited signal, which can be shown to not affect the bandlimit. In two-dimensional complex fields,

these superoscillations may be directly connected to the presence of optical vortices, lines of zero intensity in three-dimensional space around which the field has a circulating or helical structure. The creation of superoscillations may therefore be viewed as the control and manipulation of optical vortices and other field singularities. Alternatively, superoscillations in a complex field may be characterized by defining a local wavenumber that directly measures the local rate of oscillation of the field [7].

Superoscillations have already been considered as a method to break the resolution limit of traditional optical imaging systems, and superoscillatory lenses have been studied both experimentally and theoretically [8,9,10,11]. The use of superoscillations in imaging is typically limited, however, by high intensity sidelobes that accompany the subwavelength superoscillatory spot, and the intensity of the sidelobes increases as the width of the central spot is decreased.

Much more recently, researchers have begun studying the behavior of superoscillations in fields possessing random fluctuations, i.e. partial coherence. Partially coherent fields have been studied and shown promise in several applications ranging from enhancing image quality in microscopy[12], to propagation through turbulent atmosphere [13], to laser collimation[14]. However, when it comes to superoscillations, partial coherence is a relatively untouched parameter. When the spatial coherence of a field is reduced, zeros of intensity typically disappear [15], which suggests that the superoscillatory behavior breaks down. Several studies have analyzed the effect of noise on a superoscillatory signal, and have quantified the sensitivity of superoscillations to random fluctuations [16,17].

Though coherent optical vortices disappear as the coherence is decreased, analogous structures can appear in the correlation functions of partially coherent fields. These correlation vortices, or coherence vortices, appear in the phase of a two-point correlation function when one observation point is fixed[18,19]; it has also been recognized that coherent optical vortices evolve into correlation vortices as the spatial coher-

ence of a vortex beam is decreased, making them, and possibly any superoscillations associated with them, significantly more robust. Quite recently, researchers showed theoretically that some methods of randomizing superoscillatory fields will weaken the superoscillations (i.e. reduce the local frequency), while others will in fact strengthen the superoscillations [20]. Furthermore, it was shown that the intensity can increase in the neighborhood of partially coherent superoscillations, potentially making them more useful for applications.

To continue this analysis of superoscillations in partially coherent fields, it is natural to examine the effect that propagation has on the superoscillatory behavior; the 2021 paper [20] considered only fields in the source plane. In 2006, Berry and Popescu used the famous Talbot effect to study the stability of superoscillations on propagation when the source Talbot grating is the canonical superoscillatory function [21]. In that work, the authors looked at the survival of superoscillations in the Talbot effect when non-paraxial contributions to the field are considered.Superoscillations and the Talbot effect have also been recently studied with their relation to the evolution of Dirac Combs[22]. Here, we use the paraxial form of the Talbot effect and investigate how superoscillations of the Talbot grating manifest in the correlation function of the Talbot images. Previous work studying the effect of partial coherence in the Talbot effect has focused on the change in the intensity of the Talbot carpet [23]. Using the correlation function, we draw some conclusions regarding the relationship of superoscillations, propagation, and partial coherence.

We begin by briefly reviewing the relevant physics of the Talbot effect, then discuss the introduction of superoscillations and partial coherence into the Talbot effect. We then describe the results of simulations of partially coherent Talbot superoscillations.

2.2 The Talbot effect and superoscillations

This paper primarily focuses on the Talbot effect in the canonical superoscillatory function, and so we first review both of these phenomena and their combination.

The Talbot effect is often described as the "self-imaging" of a diffraction grating. At a multiple of a fixed distance from the grating, referred to as the Talbot distance, the diffracted light forms an image of the grating itself. Assuming a thin grating, its effect on an illuminating field can be described by a transmission function $t(x)$, given by

$$t(x) = \sum_{n=\infty}^{\infty} c_n \exp\left[\frac{i2\pi nx}{L}\right], \tag{2.1}$$

where the Fourier coefficients of the grating c_n are given by the integral,

$$c_n = \frac{1}{L}\int_0^L t(x') \exp\left[\frac{-i2\pi nx'}{L}\right] dx'. \tag{2.2}$$

Let us assume a quasi-monochromatic field of free-space wavenumber k_0 is illuminating the grating. For a normally incident plane wave, the field immediately after the grating is simply given by $U_0(x) = t(x)$, and represents the field in a spatial frequency decomposition.

The field at any propagation distance z can be determined using the angular spectrum representation, where each plane wave is propagated separately, with

$$U(x,z) = \sum_{n=\infty}^{\infty} c_n \exp\left[\frac{i2\pi nx}{L}\right] \exp\left[ik_z z\right], \tag{2.3}$$

where

$$k_z = \sqrt{k_0^2 - (2\pi n/L)^2}. \tag{2.4}$$

Assuming that the grating period is sufficiently large, we may apply the paraxial form of k_z and simplify it to the form,

$$k_z \approx k_0 - \frac{2\pi^2 n^2 z}{k_0 L^2}, \tag{2.5}$$

resulting in the propagation formula

$$U(x,z) = \exp[ik_0 z] \sum_{n=\infty}^{\infty} c_n \exp\left[\frac{i2\pi nx}{L}\right] \exp\left[-\frac{i2\pi^2 n^2 z}{k_0 L^2}\right]. \tag{2.6}$$

It can be readily seen that the rightmost complex exponential will be unity at distances which are a multiple of z_T, called the Talbot distance, and given by

$$z_T = \frac{k_0 L^2}{\pi}. \tag{2.7}$$

At these special distances, the field $U(x, z_T)$ exactly reproduces the field $U_0(x)$ at the grating. It can also be shown that at half the Talbot distance, the field is an exact copy of the grating field, but shifted half a period.

When the illuminating field is a tilted plane wave, with transverse wavenumber k_x, the Talbot pattern undergoes nontrivial changes [24]. We can incorporate this into the above formulas by now assuming that the field immediately after the grating is $U_0(x) = t(x)\exp[ik_x x]$, resulting in the expression

$$\begin{aligned} U(x,z) &= \exp[ik_0 z]\exp[-ik_x^2 z/2k_0]\exp[ik_x x] \\ &\times \sum_{n=\infty}^{\infty} c_n \exp\left[\frac{i2\pi nx}{L}\right] \exp\left[-\frac{i2\pi^2 n^2 z}{k_0 L^2}\right] \exp\left[-\frac{4\pi i n k_x z}{2k_0 L}\right]. \end{aligned}$$

We will have need of this formula in deriving the partially coherent Talbot effect in the next section.

It is to be noted that the paraxial propagation term $\exp[ik_0 z]$ does not affect the position of any phase singularities in the field, nor the behavior of superoscillations in the transverse plane. We will leave this term out of our calculations going forward, to simplify the phase plots.

We will use the canonical superoscillatory function as our transmission function

$t(x)$. This canonical function is given by the expression

$$t(x) = \left[\cos(\frac{\pi x}{L}) + ia\sin(\frac{\pi x}{L})\right]^N, \tag{2.8}$$

where $a > 1$ and $N \gg 1$; the quantity N represents the number of oscillations in the superoscillatory area, and a represents the degree of superoscillation. If N is even, the period of the function is L. As discussed by Berry and Popescu [21], this function possesses a maximum spatial frequency $N\pi/L$, but possesses regions where the local wavenumber oscillates at $N\pi a/L$, larger than the maximum. Provided $N\pi a/L$ is greater than the free-space wavenumber k_0, a field normally incident upon this superoscillatory grating will produce oscillations beyond the wave bandlimit at the Talbot distance.

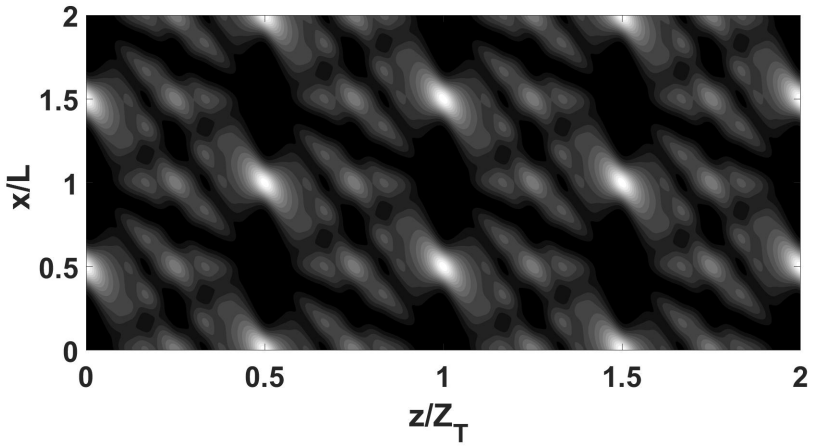

Figure 2.1: The intensity view of the Talbot carpet containing superoscillations directly after the grating, with $a = 8$, $N = 10$, $\lambda = 0.5\mu m$, $L = 4\mu m$.

An example of the intensity pattern of a superoscillatory Talbot carpet is shown in Figure 2.1, for a normally incident plane wave. For this example, and those that follow, we have taken $a = 8$, $N = 10$, $\lambda = 0.5\mu m$, $L = 4\mu m$. For these choices, the maximum Fourier spatial frequency of the grating is $k_{max} = 7.85\mu m^{-1}$, and the maximum local superoscillatory frequency is $k_{so} = 62.8\mu m^{-1}$; the wavenumber is $k_0 = 12.6\mu m^{-1}$. It can be seen that the intensity pattern is reproduced at the

Talbot distance and the half Talbot distance. At other fractional Talbot distances, higher spatial frequency copies of the original pattern can be seen, corresponding to the fractional Talbot effect [25]. We will focus on the effect of spatial coherence on the superoscillations at the Talbot and half Talbot distance. It is valuable to note that through the Talbot effect, we see replications of the superoscillations along the propagation axis. This is analogous, though quite different to the revival of supperoscilations along propagation through an absorbing media shown in [26].

2.3 Partially coherent superoscillations and the Talbot effect

We now consider the effects of spatial coherence on the system and its superoscillations. The standard quantity used to characterize spatial coherence is the cross-spectral density, defined as [27]

$$W(\mathbf{r}_1, \mathbf{r}_2, \omega) = \langle U^*(\mathbf{r}_1, \omega) U(\mathbf{r}_2, \omega) \rangle_\omega, \tag{2.9}$$

where $\langle \cdots \rangle_\omega$ represents an average over a statistical ensemble of monochromatic fields, and in our case $\mathbf{r} = (x, z)$. We will be working with quasi-monochromatic fields, which can be well-approximated by their behavior at a single frequency, and will suppress ω as an explicit argument going forward.

We consider a system where the Talbot grating is illuminated by a partially coherent plane wave with cross-spectral density in the plane $z = 0$ of the form

$$W_0(x_1, x_2) = S_0 \exp[-(x_2 - x_1)^2 / 2\sigma_g^2], \tag{2.10}$$

where S_0 is the average spectral density (intensity) and σ_g is the correlation length. This correlation function may be written in a Fourier representation as

$$W_0(x_1, x_2) = \int_{-\infty}^{\infty} \tilde{W}_0(k_x) \exp[ik_x(x_2 - x_1)] dk_x. \tag{2.11}$$

In this form, the cross-spectral density is expressed as the average over an ensemble of tilted plane waves, with the probability density

$$\tilde{W}_0(k_x) = \frac{1}{2\pi}\int_{-\infty}^{\infty} W_0(x)e^{-ik_x x}dx = \frac{S_0\sigma_g}{\sqrt{2\pi}}\exp\left[-k_x^2\sigma_g^2/2\right]. \tag{2.12}$$

The constant factor plays no role in the properties of superoscillations. We introduce $\sigma_k \equiv 1/\sigma_g$ for convenience, and write

$$\tilde{W}_0(k_x) = \exp[-k_x^2/2\sigma_k^2]. \tag{2.13}$$

Following Berry and Popescu [21], the transmission function of the superoscillatory grating may be written in the form,

$$t(x) = \sum_{m=0}^{N} c_m \exp\left[\frac{iN\pi V_m x}{L}\right], \tag{2.14}$$

$$C_m = \frac{N!}{2^N}(-1)^m \frac{(a^2-1)^{N/2}\left[\frac{a-1}{a+1}\right]^{\frac{NV_m}{2}}}{\left[\frac{N(1+V_m)}{2}\right]!\left[\frac{N(1-V_m)}{2}\right]!}, \tag{2.15}$$

with

$$V_m = 1 - \frac{2m}{N}. \tag{2.16}$$

On propagation, the expression for a field with transverse wavenumber k_x may be found from Eq. (2.8) to be of the form,

$$U(x,z) = \sum_{m=0}^{N} c_m \exp\left[i\left(\frac{N\pi V_m}{L} + k_x\right)x\right]\exp\left[-i\frac{z}{2k_0}\left(NV_m\pi/L + k_x\right)^2\right],$$

where again we note that the trivial propagation term $\exp[ik_0 z]$ has been neglected. This field may be substituted twice into Eq. (2.11), and the integral over k_x can be evaluated analytically. The final result for the cross-spectral density may be written as

$$W(x_1, x_2, z_1, z_2) = \sqrt{\frac{\pi}{1/2\sigma_k^2 + i(z_2 - z_1)/2k_0}}$$
$$\times \sum_{m,n} c_m^* c_n \exp[iN\pi(V_n x_2 - V_m x_1)/L]$$
$$\times \exp[iN^2\pi^2(V_m^2 z_1 - V_n^2 z_2)/2k_0 L^2]$$
$$\times \exp\left[-\frac{\left[\frac{N\pi}{k_0 L}(z_2 V_n - z_1 V_m) + (x_1 - x_2)\right]^2}{2/\sigma_k^2 + 2i(z_2 - z_1)/k_0}\right].$$

This calculation is described in more detail in Appendix A. The main effect of the source coherence on the field propagation is found in the final exponential in this expression.

It is to be noted that the introduction of partial coherence stretches the spatial frequency spectrum of the propagated field, and because that spectrum is Gaussian it is no longer strictly bandlimited. In this case, the system should be viewed as one with superoscillations with a "leaky" spectrum, as discussed by Berry [28]. To justify calling the structures in our system "superoscillations," we note that the largest value $\sigma_k = 0.027\mu m^{-1}$ used in our simulations is significantly smaller than the largest spatial frequency of the grating, which is $7.85\mu m^{-1}$ for the parameters given below. The amount of energy in the high spatial frequency of the tails of the Gaussian is therefore negligible and unlikely to contribute to the superoscillations. Furthermore, the structures we see in the partially coherent case can be traced directly to the superoscillations of the fully coherent case, which is bandlimited. Our partially coherent oscillations may therefore be considered the natural extension of coherent superoscillations.

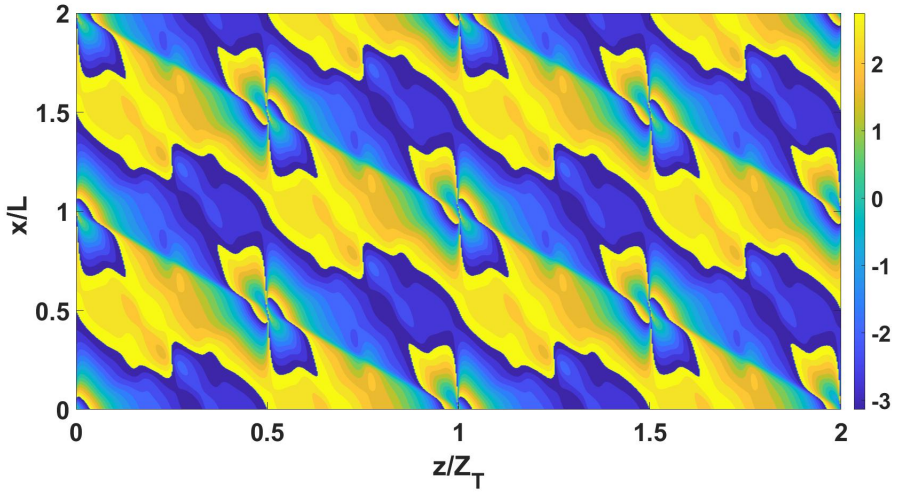

Figure 2.2: Phase plot of a Talbot carpet containing superoscillations at the primary and secondary Talbot images, with $x_1 = 2\mu m$, $z_1 = 0.5z_T$, and $\sigma_k = 0.001\mu m^{-1}$.

2.4 Superoscillations and partial coherence

As noted in the Introduction, the intensity zeros of a coherent wavefield typically disappear as the spatial coherence of the field is decreased. However, the associated singularities persist as singularities in the two-point cross-spectral density. These zeros will appear as edge dislocations in the phase plots of the cross-spectral density in $\mathbf{r}_2$ when observation point $\mathbf{r}_1$ is fixed. We now consider how the zeros of the cross-spectral density evolve as the spatial coherence is decreased, and the relationship to the superoscillatory nature of the field. In all these examples, we use $a = 8$, $N = 10$, $\lambda = 0.5\mu m$, $L = 4\mu m$.

Figure 2.2 shows an example of the phase structure of a field over two Talbot distances. Here, the observation point is taken as $x_1 = 2\mu m$, $z_1 = 0.5z_T$, and $\sigma_k = 0.001\mu m^{-1}$, or $\sigma_g = 1mm$, representing a highly coherent field. Edge dislocations of the cross-spectral density are located where all the phase colors converge at a point. The only singularities that exist are located near the Talbot distance and the half-Talbot distance; we will see that they are important in producing the superoscillatory behavior.

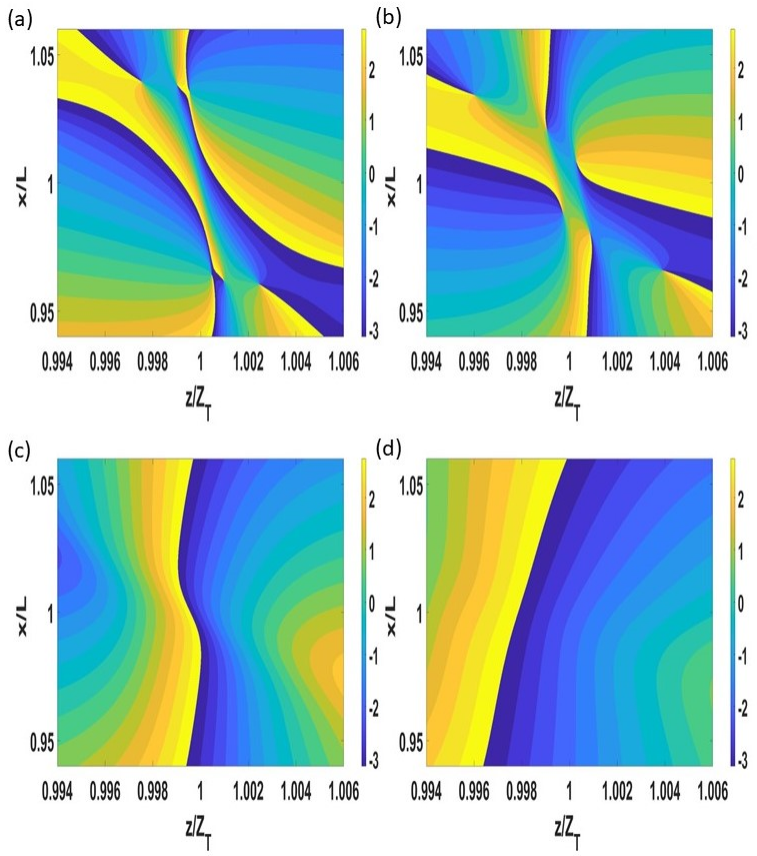

Figure 2.3: Detail of the phase structure of the cross-spectral density around $z = z_T$ as the spatial coherence is decreased, with (a) $\sigma_k = 0.002\mu m^{-1}$ (b) $\sigma_k = 0.014\mu m^{-1}$, (c) $\sigma_k = 0.027\mu m^{-1}$, (d) $\sigma_k = 0.04\mu m^{-1}$. Again we have $x_1 = 2\mu m$, $z_1 = 0.5 z_T$.

As spatial coherence is decreased, it is expected that the detailed Talbot intensity pattern will blur on propagation, and the singularities of the cross-spectral density will change positions, affecting the superoscillatory structure. This behavior will be distance-dependent: at larger multiples of the Talbot distance, the decrease in coherence will have a stronger effect than at smaller multiples. Figure 2.3 shows the detailed phase structure in the neighborhood of the singularities at the Talbot distance for different values of σ_k. It is to be noted that the zeros are not in the plane $z = z_T$; the rapid change of phase associated with the superoscillations arises from the rapid change of phase in the vicinity of an edge dislocation.

As the spatial coherence is decreased, the singularities come together and eventually

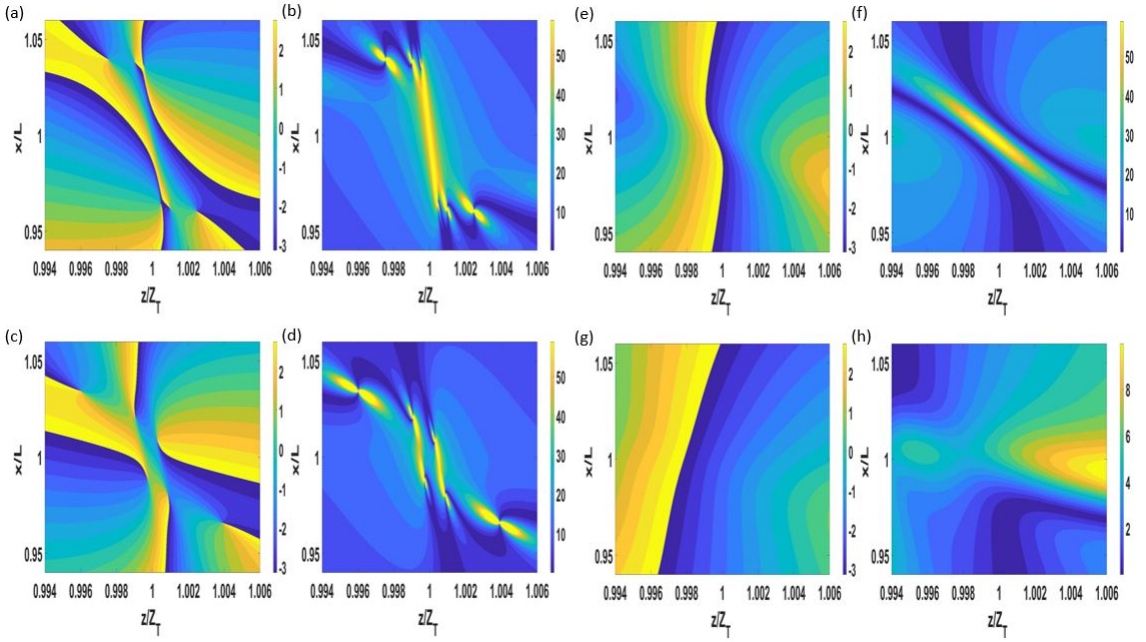

Figure 2.4: A comparison of the phase of the cross-spectral density shown in figure 2.3 with their corresponding local wavenumber. with $x_1 = 2\mu m$, $z_1 = 0.5z_T$, and (a,b) $\sigma_k = 0.002\mu m^{-1}$, (c,d)$\sigma_k = 0.014\mu m^{-1}$ (e,f), $\sigma_k = 0.027\mu m^{-1}$ (g,h), $\sigma_k = 0.04\mu m^{-1}$.

annihilate. This suggests that the superoscillations become more rapid at first, but eventually break down when the singularities themselves vanish.

A more quantitative measure of the strength of superoscillations in a complex wavefield is the local wavenumber. We consider only the transverse local wavenumber, defined by the expression,

$$k(\mathbf{r}_1, \mathbf{r}_2) = \left| Im \frac{\partial_{x_2} W(\mathbf{r}_1, \mathbf{r}_2)}{W(\mathbf{r}_1, \mathbf{r}_2)} \right|. \tag{2.17}$$

Figure 2.4 shows a comparison of the phase of the cross-spectral density and the local wavenumber as the spatial coherence is decreased. The singularities can be seen to correspond to regions of high local wavenumber. As the spatial coherence is decreased, the singularities come together and the local wavenumber becomes correspondingly larger, but decreases dramatically as the singularities annihilate.

It is worth noting that there seems to be some vagueness in the literature about

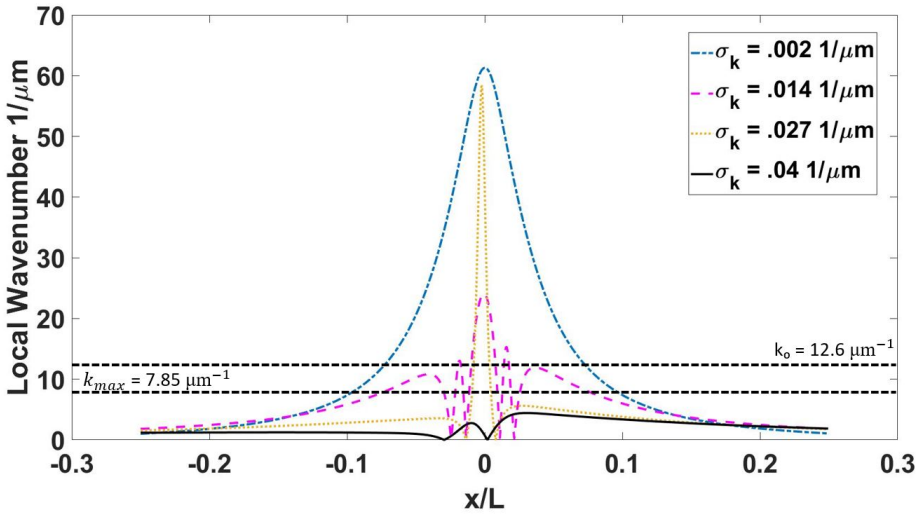

Figure 2.5: The local wavenumber at the Talbot Distance along one grating period. This plot shows the change in local wavenumber from a fully coherent field to a high level of spatial incoherence field.

the role of zeros in superoscillations. In some work, such as Refs. [5,10,29], superoscillations are produced by the explicit positioning of zeros and the strength of superoscillations is defined by the spacing of zeros; in contrast, the canonical superoscillatory function possesses no zeros at all and the local wavenumber characterizes the rate of superoscillation. In our investigations of the Talbot effect, at least, we can see that these are two different manifestations of the same phenomenon: the high local wavenumber at the Talbot distance is produced by the nearby off-plane zeros.

Figure 2.5 shows the local wavenumber in the Talbot plane as the spatial coherence is decreased, and these plots can be compared with the phase images of Fig. 2.3 or 2.4. For a fully coherent field, the maximum value is equal to the value given by $N\pi a/L$. As the coherence decreases, the maximum of the local wavenumber decreases, but then rapidly increases again as the singularities of the cross-spectral density come together and annihilate near the Talbot plane. Once the singularities have disappeared completely, the local wavenumber is no longer superoscillatory, and is in fact lower than the grating wavenumber. We therefore see that there is a range of coherence values for which the cross-spectral density is more superoscillatory than

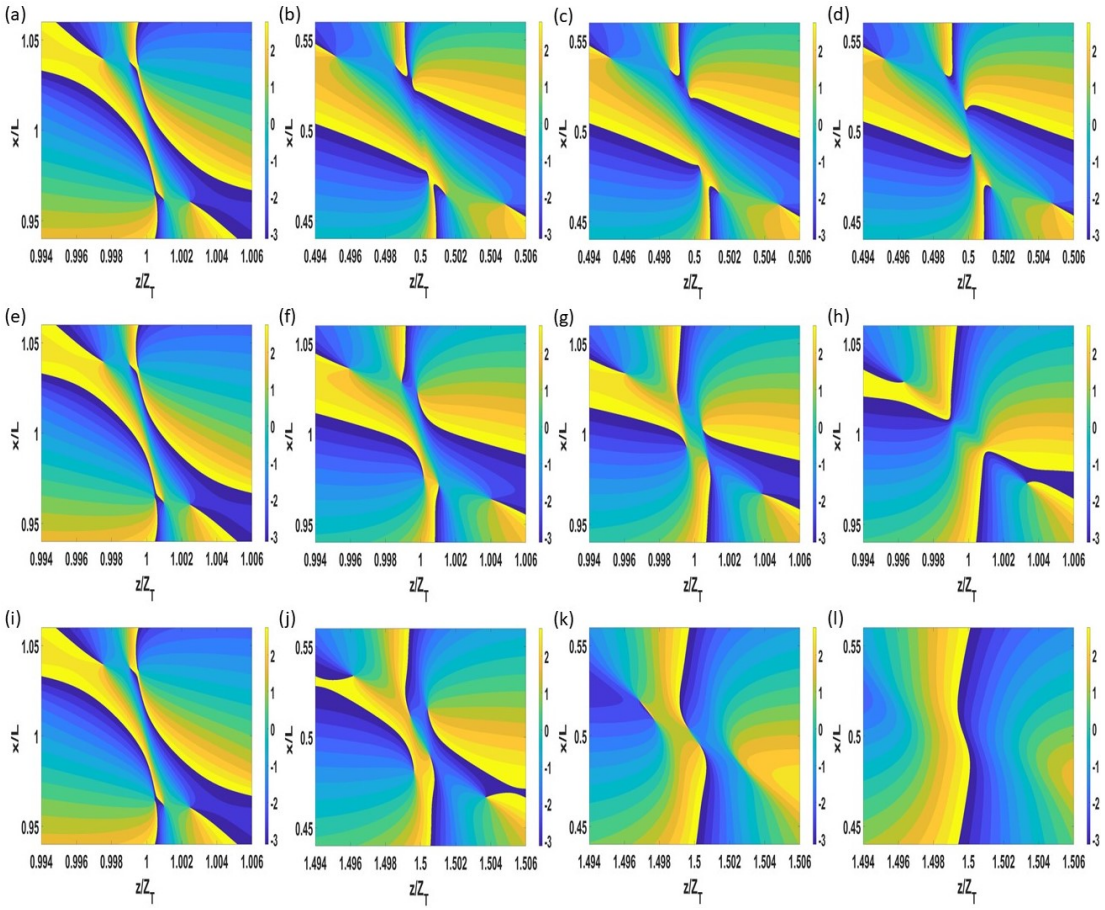

Figure 2.6: The phase of the cross-spectral density for different propagation distances and states of coherence. (a,b,c,d) $z = 0.5z_T$, (e,f,g,h) $z = z_T$, (i,j,k,l) $z = 1.5z_T$. First column: $\sigma_k = 0.002\mu m^{-1}$, second column: $\sigma_k = 0.012\mu m^{-1}$, third column: $\sigma_k = 0.016\mu m^{-1}$, fourth column: $\sigma_k = 0.02\mu m^{-1}$.

the corresponding fully coherent field.

For partially coherent fields, the superoscillatory behavior also decays with propagation distance. As Eq. (2.11) demonstrates, partial coherence can be interpreted as an incoherent superposition of plane waves propagating in different directions, resulting in an incoherent superposition of different tilted Talbot patterns. As the propagation distance increases and/or the spatial coherence decreases, these different Talbot patterns become out of step, blurring the overall pattern and eventually annihilating the singularities in the correlation function. In the $z = 0$ plane, the canonical superoscillatory function is always present, since the coherence is only a multiplicative

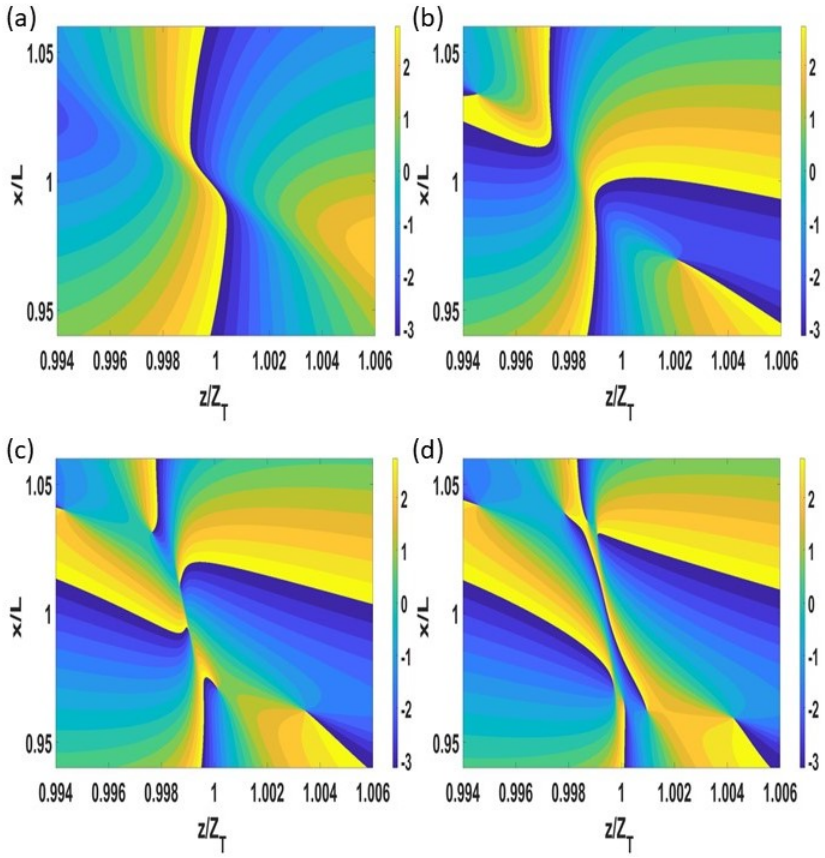

Figure 2.7: The phase of the cross-spectral density as the observation point is moved. For these plots $x_1 = 2\mu m$, $\sigma_k = .027\mu m^{-1}$, and z_1 is (a)$0.5z_T$ (b)$6.5z_T$ (c)$12.5z_T$ and (d)$25.5z_T$.

factor with the transmission function; at increasing multiples of the Talbot distance, we expect to see coherence play a stronger role.

Figure 2.6 shows the phase behavior at several primary and secondary Talbot distances, as a function of decreasing coherence. The trends are clear from the sequence of images: the singularities move together faster with larger propagation distance (downward in rows) and/or smaller spatial coherence (rightward in columns).

For all of the previous results, the position of the observation point has remained fixed. However, the cross-spectral density is a two-point correlation function and the location of zeros will depend on the choice of $\mathbf{r}_1$. This choice can have a significant effect: in [20], superoscillations in partially coherent beams were studied, and it was found that as the observation point was moved away from the beam center, the phase

of the superoscillatory region appeared to regress to its fully coherent state.

Figure 2.7 shows the effect of changing the observation distance z_1 further away from the grating. With the observation distance close to the image plane, the singularities, and corresponding superoscillations, are not present. As the observation point is moved very far away, the spatial coherence "revives" and the singularities reappear, with the final image looking strikingly similar to Fig. 2.3(a).

Changes in the phase structure can also be found by moving the transverse position x_1 along the grating. Due to the periodic nature of the grating, the phase plots repeat with period L.

2.5 Observations

The manipulation of spatial coherence in the superoscillatory Talbot effect provides new degrees of freedom for manipulating the strength of superoscillations, and provides new insight into the phenomenon of superoscillations in partially coherent fields. These superoscillations appear in the two-point correlation function of the field, rather than the field itself.

We have seen that, contrary to what rough intuition might suggest, superoscillatory behavior can increase as spatial coherence decreases, which corresponds to the zeros of the cross-spectral density moving closer together and annihilating. When the annihilation occurs, the superoscillatory behavior disappears.

We have seen that changes in both the spatial coherence and the observation point can dramatically affect the superoscillatory behavior at the Talbot distance. There is therefore great flexibility in tailoring these superoscillations for applications.

All of these results have been explored with an eye towards using partially coherent superoscillations in imaging applications. The possibility of having appreciable intensity in the region of superoscillations is a motivating factor. It is to be noted that an imaging system based on partially coherent superoscillations would need to be very different from a conventional imaging system, due to the use of the two-point

correlation function. An interferometric scheme would need to be used, and we are investigating how such a scheme could be implemented and any benefits it might provide. Our work on the partially coherent superoscillatory Talbot effect gives us insight into the expected features of the imaging field.

REFERENCES

[1] M.V. Berry. Faster than Fourier. In J.S. Anandan and J.L. Safko, editors, *Proceedings of the International Conference on Fundamental Aspects of Quantum Theory*, pages 55-65, Singapore, 1995. World Scientific.

[2] Michael Berry, Nikolay Zheludev, Yakir Aharonov, Fabrizio Colombo, Irene Sabadini, Daniele C Struppa, Jeff Tollaksen, Edward T F Rogers, Fei Qin, Minghui Hong, Xiangang Luo, Roei Remez, Ady Arie, Mark R Dennis, Alex M H Wong, George V Eleftheriades, Yaniv Eliezer, Alon Bahabad, Gang Chen, Zhongquan Wen, Gaofeng Liang, Chenglong Hao, C-W Qiu, Achim Kempf, Eytan Katzav, and Moshe Schwartz. Roadmap on superoscillations. *Journal of Optics*, 21(5):053002, apr 2019.

[3] G. Gbur. Using superoscillations for superresolved imaging and subwavelength focusing. *Nanophotonics*, 8(2):205 - 225, 01 Feb. 2019.

[4] Y. Aharonov, F. Colombo, I. Sabadini, D. C. Struppa, and J. Tollaksen. The mathematics of superoscillations, 2015.

[5] I. Chremmos and G. Fikioris. Superoscillations with arbitrary polynomial shape. *Journal of Physics A: Mathematical and Theoretical*, 48(26):265204, jun 2015.

[6] M.K. Smith and G. Gbur. Construction of arbitrary vortex and superoscillatory fields. *Opt. Lett.*, 41(21):4979-4982, Nov 2016.

[7] Mark R. Dennis, Alasdair C. Hamilton, and Johannes Courtial. Superoscillation in speckle patterns. *Opt. Lett.*, 33(24):2976-2978, Dec 2008.

[8] Fu Min Huang, Yifang Chen, F.Javier Garcia de Abajo, and Nikolay I. Zheludev. Optical super-resolution through super-oscillations. *Journal of Optics A: Pure and Applied Optics*, 9(5):S285-S288, September 2007.

[9] E.T.F. Rogers, J. Lindberg, T. Roy, S. Savo, J.E. Chad, M.R. Dennis, and N.I. Zheludev. A superoscillatory lens optical microscope for subwavelength imaging. *Nature Materials*, 11:432-435, 2012.

[10] Reza K. Amineh and George V. Eleftheriades. 2d and 3d sub-diffraction source imaging with a superoscillatory filter. Opt. Express, 21(7):8142-8157, Apr 2013.

[11] M.K. Smith and G. Gbur. Mathematical method for designing superresolution lenses using superoscillations. *Opt. Lett.*, 45(7):1854-1857, Apr 2020.

[12] Yoon Bae, Martin Sohn, Dong-Ryoung Lee, and Sang-Soo Choi. Effect of partial coherence on dimensional measurement sensitivity for DUV scatterfield imaging microscopy. (27), 2019-10-02 00:10:00 2019.

[13] Greg Gbur. Partially coherent beam propagation in atmospheric turbulence [invited]. *J. Opt. Soc. Am. A*, 31(9):2038-2045, Sep 2014.

[14] W. S. C. Chang and N. R. Kilcoyne. A study of partial coherence and its application to the collimation of pulsed multimode laser radiation. *Appl. Opt.*,4(11):1404-1411, Nov 1965.

[15] G.Gbur, T.D. Visser, and E. Wolf. hidden singularities in partially coherent wavefields. *Journal of Optics A: Pure and Applied Optics*, 6(5):S239-S242, apr 2004.

[16] M.V. Berry. Suppression of superoscillations by noise. *Journal of Physics A: Mathematical and Theoretical*, 50(2):025003, dec 2017.

[17] E. Katzav, E. Perlsman, and M. Schwartz. Yield statistics of interpolated superoscillations. *Journal of Physics A: Mathematical and Theoretical*, 50(2):025001, dec 2017.

[18] I.D. Maleev, D.M. Palacios, A.S. Marathay, and G.A. Swartzlander, Jr. Spatial correlation vortices in partially coherent light: theory. *J. Opt. Soc. Am. B*, 21:1895-1900, 2004.

[19] D.M. Palacios, I.D. Maleev, A.S. Marathay, and Jr.G.A. Swartzlander. Spatial correlation singularity of a vortex field. *Phys. Rev. Lett.*, 92:143905, 2004.

[20] Joseph Mays and Greg Gbur. Superoscillatory behavior in partially coherent fields. *Journal of Optics*, 23(7):074002, jun 2021.

[21] M V Berry and S Popescu. Evolution of quantum superoscillations and optical superresolution without evanescent waves. *Journal of Physics A: Mathematical and General*, 39(22):6965-6977, may 2006.

[22] Fabrizio Colombo, Irene Sabadini, Daniele C. Struppa, and Alain Yger. Gauss sums, superoscillations and the talbot carpet. *Journal de Mathematiques Pures et Appliquees*, 147:163-178, 2021.

[23] Shuyun Teng, Liren Liu, Jifeng Zu, Zhu Luan, and De'an Liu. Uniform theory of the talbot effect with partially coherent light illumination. *J. Opt. Soc. Am. A*, 20(9):1747-1754, Sep 2003.

[24] Markus Testorf, Jurgen Jahns, Nikolay A. Khilo, and Andrey M. Goncharenko. Talbot effect for oblique angle of light propagation. *Optics Communications*, 129(3-4):167-172, February 1996.

[25] M. V. Berry and S. Klein. Integer, fractional and fractal talbot effects. *Journal of Modern Optics*, 43(10):2139-2164, 1996.

[26] Yaniv Eliezer and Alon Bahabad. Super-transmission: the delivery of superoscillations through the absorbing resonance of a dielectric medium. *Opt. Express*, 22(25):31212-31226, Dec 2014.

[27] E. Wolf. New theory of partial coherence in the space-frequency domain. part 1: spectra and cross-spectra of steady-state sources. *J. Opt. Soc. Am.*, 72:343-351, 1982.

[28] M V Berry. Superoscillations and leaky spectra. *Journal of Physics A: Mathematical and Theoretical*, 52(1):015202, nov 2018.

[29] W. Qiao. A simple model of Aharonov-Berry's superoscillations. *J. Phys. A,* 29:2257-2258, 1996.

[30] I. S. Gradshteyn and I. M. Ryzhik. *Table of integrals, series, and products.* Elsevier/Academic Press, Amsterdam, seventh edition, 2007. equation 3.323.

APPENDIX: Cross-spectral Density of the Superoscillatory Talbot Effect

In this appendix, we derive the partially coherent cross-spectral density for a superoscillatory Talbot field shown in equation 2.17 beginning at the propagated field 2.17. As stated we can substitute the propagated field into our cross-spectral density given by:

$$W(x_1, x_2, z_1, z_2) = S_0 \int_{-\infty}^{\infty} \tilde{\mu}_0(k_{x0}) \tilde{U}_{kx}(x_1, z_1) U_{kx}(x_2, z_2) dk_{x0}. \tag{2.18}$$

With this substitution, we now have our cross-spectral density of the form

$$\begin{aligned} W(x_1, x_2, z_1, z_2) = & \sum_{m,n} \int_{-\infty}^{\infty} \tilde{\mu}_0(k_x) c_m^* c_n \\ & \times \exp[-ix_1(NV_m\pi/L + k_x)] \exp[ix_2(NV_n\pi/L + k_x)] \\ & \times \exp\left[\frac{-iz_1}{2k_0}(NV_m\pi/L + k_x)^2\right] \exp\left[\frac{-iz_2}{2k_0}(NV_n\pi/L + k_x)^2\right] dk_x, \end{aligned} \tag{2.19}$$

where:

$$\tilde{\mu}_0(k_x) = \exp\left[\frac{-k_{x0}^2}{2\sigma_k^2}\right]. \tag{2.20}$$

Pulling out the independent terms, we can establish the integral from the cross-spectral density to be:

$$W(x_1, x_2, z_1, z_2) = \sum_{m,n} c_m^* c_n \exp[iN\pi(V_n x_2 - V_m x_1)/L] \left[\exp \frac{iN^2\pi^2(V_m^2 z_1 - V_n^2 z_2)}{2k_0 L^2}\right]$$
$$\int_{-\infty}^{\infty} \exp\left[\frac{-k_x^2}{2\sigma_k^2}\right] \exp\left[\frac{ik_x^2}{2k_0}(z_1 - z_2)\right] \exp\left[\frac{i\pi k_x N}{k_0 L}(z_1 V_m - z_2 V_n)\right] \exp[ik_x(x_2 - x_1)] dk_x.$$

This is of a similar for to a known integral identity [30]:

$$\int_{-\infty}^{\infty} \exp(-p^2x^2 + qx) dx = \sqrt{\frac{\pi}{p^2}} \exp\left[\frac{q^2}{4p^2}\right]; Rep^2 > 0, \tag{2.21}$$

where:

$$p^2 = 1/2\sigma_k^2 + i(z_2 - z_1)/2k_0, \tag{2.22}$$

and

$$q = \frac{iN\pi}{k_0 L}(z_2 V_n - z_1 V_m) + (x_1 - x_2). \tag{2.23}$$

Utilizing this identity, the integral is found to have the form:

$$\sqrt{\frac{\pi}{1/2\sigma_k^2 + i(z_2 - z_1)/2k_0}} \exp\left[-\frac{\left[\frac{N\pi}{k_0 L}(z_2 V_n - z_1 V_m) + (x_1 - x_2)\right]^2}{2/\sigma_k^2 + 2i(z_2 - z_1)/k_0} \right]. \tag{2.24}$$

We can now take this integral solution and recombine it back into the cross-spectral density. Doing this and then combining all of the like terms will give us equation 2.17.

CHAPTER 3: Angular Momentum of Vector Twisted Vortex Gaussian-Schell Model Beams

ABSTRACT

We generalize a recently-introduced class of partially coherent vortex beams known as Twisted Vortex Gaussian-Schell Model Beams. Through the addition of spatially-varying polarization, we create a beam whose angular momentum is provided from three different sources: the underlying vortex order of the beam, the "twist" given to the ensemble of beams, and the circular polarization of the beam. The combination of these angular momentum types allows for unprecedented control over the total angular momentum of the field and its transverse distribution.

3.1 Introduction

Singular optics is a branch of physical optics that encompasses the study of the topological singularities of light. This field has grown grown in significance dramatically over the past few decades, and in recent years many of these topological phenomena have begun showing their relevance in practical application [1,2,3]. The most well known of these phenomena are optical vortices. An optical vortex in a field is a line in three-dimensional space upon which the intensity is zero and the phase is consequently undefined, i.e. singular. The phase has a circulating or helical structure around the zero line, and increases or decreases by a multiple of 2π. In a cross-section of a field, vortices typically manifest as a point of zero intensity. These vortices and their structures have found relevance in several optical applications including encoding information and overcoming turbulence in optical communications [4,5], reducing scattering in underwater laser detection and ranging systems [6,7], and

optical tweezing [8].

A beam with a pure optical vortex in its core has a definite handedness, and consequently possesses orbital angular momentum (OAM); if the polarization properties of the beam are also considered, it may also possess spin angular momentum (SAM). The aforementioned optical tweezing uses these beams to impart controlled, small forces upon particles through momentum transfer. Angular momentum is also employed in free space optical communication (FSOC) [9]. Information can be encoded and multiplexed in distinct angular momentum modes, significantly increasing the rate of data transmission. But over long propagation paths in atmospheric turbulence, the turbulence distorts the phase structure of the field, causing signal degradation and mode crosstalk [10].

One possible solution to this degradation is the use of partially coherent beams; such beams have been shown in many cases to provide resistance to turbulence distortion [11]. A number of classes of partially coherent beams possessing OAM have been introduced, including twisted Gaussian Schell-model beams [12] and what are now called Rankine vortex beams [13]. Much more recently, a new class of beams was introduced, referred to as twisted vortex Gaussian Schell-model beams (tvGSM), which possess both a phase vortex and a partially coherent twist [14]. These beams can be constructed through the combination of a Rankine vortex beam and a twisted Gaussian Schell-model beam (tGSM) utilizing a superposition model. The superposition model consists of an ensemble of modes incoherently combined to produce the cross-spectral density. For the Rankine beam, the ensemble is a set of vortex modes. For the tGSM beam, the ensemble is a set of tilted Gaussian modes. Both of these beams have distinct orbital angular momentum properties. The tGSM beam acts similarly to a rigid body rotator and the Rankine beam behaves like a Rankine vortex [15].

The tvGSM beams have their OAM arise from two distinct origins: the discrete

coherent phase vortex and the continuous partially coherent twist. This combination provides unprecedented control over the OAM, as shown in Ref. [14]. Because an electromagnetic beam will also possess spin angular momentum, it is natural to next investigate how the addition of spin can change and enhance the control of angular momentum in a partially coherent beam.

As will be shown, through the incorporation of adjustable non-uniform polarization into tvGSM beams, we now have a third degree of freedom for manipulating angular momentum along with vortex order and twist parameter. With these three tunable parameters, such vector tvGSM (vtvGSM) beams provide remarkable control over the distribution of angular momentum in the beam's cross-section.

3.2 Vector TVGSM Model

To study beams that possess rapid random fluctuations, it is necessary to characterize the average properties of the field. We will do this through use of the cross-spectral density function, which can be defined as [16]

$$W(\mathbf{r}_1, \mathbf{r}_2, \omega) = \langle \tilde{U}(\mathbf{r}_1, \omega) U(\mathbf{r}_2, \omega) \rangle_\omega, \tag{3.1}$$

where $U(\mathbf{r}, \omega)$ represents a monochromatic scalar field and $\langle \cdots \rangle_\omega$ represents an average over an ensemble of monochromatic fields. For convenience, we use a tilde to represent the complex conjugate throughout the paper. The cross-spectral density characterizes the spatial coherence properties of the field at frequency ω; for quasi-monochromatic fields, the behavior of the beam as a whole can be well-described by the behavior at the central frequency. We consider such a case, and suppress ω going forward for brevity.

We consider ensemble averages over a spatial variable $\mathbf{r}_0$ of the form

$$W_{pq}(\mathbf{r}_1, \mathbf{r}_2) = \int \tilde{U}_p(\mathbf{r}_1, \mathbf{r}_0) U_q(\mathbf{r}_2, \mathbf{r}_0) P(\mathbf{r}_0) d^2\mathbf{r}_0, \tag{3.2}$$

with $P(\mathbf{r}_0)$ being the probability density and $\mathbf{r}_0$ being a transverse position, such that

$$P(\mathbf{r}_0) = P_0 \exp\left[-\frac{(x_0^2 + y_0^2)}{\sigma^2}\right], \tag{3.3}$$

with $|\mathbf{r}_0|^2 = x_0^2 + y_0^2$ and σ represents the width of the probability function. The vector $\mathbf{r}_0$ effectively labels a member of the ensemble. In this expression, U_p and U_q represent distinct spatial modes of the field that will arise in our electromagnetic description, as we describe momentarily.

We are interested in constructing a vector partially coherent beam by building upon the design of a tvGSM beam; the construction of a vtvGSM beam follows closely the construction of the earlier model. For a more in depth derivation of the propagation terms and cross-spectral density, one can refer to Ref. [14].

We can construct a tvGSM beam by combining the models of a Rankine vortex beam and a tGSM beam. For the Rankine beam, one uses Laguerre-Gaussian beam modes of azimumthal order p,

$$U(\mathbf{r}, \mathbf{r}_0) = \frac{U_0}{\Delta^p} \exp\left[-\frac{[(x - x_0)^2 + (y - x_0)^2]}{2\Delta^2}\right] [(x - x_0) + i(y - y_0)]^p, \tag{3.4}$$

where Δ is the width of the Gaussian envelope and p is a non-negative integer. This model, which treats each member of the ensemble as having a transversely-displaced axis, was originally referred to as the 'beam wander model' [17]. For tGSM beams, one uses fundamental Gaussian modes with a position dependent tilt, of the form [12]

$$U(\mathbf{r}, \mathbf{r}_0) = U_0 \exp\left[-\frac{[(x - x_0)^2 + (y - x_0)^2]}{2\Delta^2}\right] \exp\left[2\pi i\alpha(x_0 y - y_0 x)\right], \tag{3.5}$$

where α is the "twist parameter." If we merge the two previous ensembles we get a

tvGSM beam mode of the form

$$U_p(\mathbf{r},\mathbf{r}_0) = \frac{U_0}{\Delta^p}\exp\left[-\frac{[(x-x_0)^2+(y-x_0)^2]}{2\Delta^2}\right] \times \exp\left[2\pi i\alpha(x_0y-y_0x)\right]\left[(x-x_0)+i(y-y_0)\right]^p, \tag{3.6}$$

which possesses the vortex core of the Rankine beam and the tilt of the twisted beam. By substituting from Eq. (3.6) into Eq. (3.2), the tvGSM cross-spectral density can be determined.

To incorporate non-trivial polarization into this model, we introduce an electric field ensemble of the form

$$\mathbf{E}(\mathbf{r},\mathbf{r}_0) = \Psi U_m(\mathbf{r},\mathbf{r}_0)\hat{e}_+ + (1-\Psi)U_n(\mathbf{r},\mathbf{r}_0)\hat{e}_-, \tag{3.7}$$

where

$$\hat{e}_+ = \frac{\hat{x}+i\hat{y}}{\sqrt{2}}, \quad \hat{e}_- = \frac{\hat{x}-i\hat{y}}{\sqrt{2}} \tag{3.8}$$

represent the unit vectors for left and right-hand circular polarization, respectively. The values m and n represent the particular mode orders chosen for our model; they can in fact be taken to have any non-negative integer values.

It is to be noted that we could have introduced SAM trivially into our model by making the field uniformly elliptically polarized, with the amount of SAM determined by the strength of the ellipticity. By instead using different spatial modes and weights for the circular polarization states, we create a non-trivial spatial distribution of SAM in the beam cross-section. The quantity Ψ is an adjustable polarization amplitude parameter, which allows us to emphasize one circular state or another.

Because there are now two distinct polarization states, there are four distinct correlation functions, and we must use a cross-spectral density matrix $\mathbf{W}$ to characterize the properties of the field [18]. In the circular polarization basis, this matrix takes on

the form

$$\mathbf{W}(\mathbf{r}_1,\mathbf{r}_2) = \left\langle \begin{bmatrix} \Psi^2\tilde{U}_m(\mathbf{r}_1)U_m(\mathbf{r}_2) & \Psi(1-\Psi)\tilde{U}_m(\mathbf{r}_1)U_n(\mathbf{r}_2) \\ (1-\Psi)\Psi\tilde{U}_n(\mathbf{r}_1)U_m(\mathbf{r}_2) & (1-\Psi)^2\tilde{U}_n(\mathbf{r}_1)U_n(\mathbf{r}_2) \end{bmatrix} \right\rangle. \tag{3.9}$$

It is at this point that we apply Appendix A of Ref. [14] to evaluate the propagation of $U_m(\mathbf{r},\mathbf{r}_0)$ and $U_n(\mathbf{r},\mathbf{r}_0)$ so that they can be substituted into Eq. (3.2). Following that Appendix, a mode $U_p(\mathbf{r},\mathbf{r}_0)$ at any distance z can be written as

$$\begin{aligned} U_p(\mathbf{r},\mathbf{r}_0,z) =& \frac{U_0}{\beta} exp[ik_0 z] \frac{[(x+iy)-(1+i\gamma)(x_0+iy_0)]^p}{(\Delta\beta)^p} \\ & \times exp\left[|\mathbf{r}-\mathbf{r}_0|^2/(2\Delta^2\beta)\right] exp\left[-|\mathbf{r}_0|^2\frac{i\pi\alpha\gamma}{\beta}\right] \\ & \times exp\left[(yx_0-xy_0)\frac{2i\pi\alpha}{\beta}\right], \end{aligned} \tag{3.10}$$

where

$$\beta \equiv 1 - \frac{z}{ik\Delta^2}, \tag{3.11}$$

and

$$\gamma \equiv \frac{2\pi\alpha z}{k_0}. \tag{3.12}$$

We may substitute from Eq. (3.10) into Eq. (3.2) to get the explicit form of the cross-spectral density matrix; this derivation is lengthy but straightforward. We find that each element of the cross-spectral density matrix at any distance z may be written as

$$W_{pq}(\mathbf{r}_1,\mathbf{r}_2,z) = C_{pq}(z)F(\mathbf{r}_1,\mathbf{r}_2,z)\sum_{k=0}^{\min(p,q)}\binom{p}{k}\binom{q}{k}\frac{\Gamma(k+1)}{A^{2(k-p-q)-2}}D_1^{p-k}D_2^{q-k}, \tag{3.13}$$

where $\min(p,q)$ represents the minimum value of p and q. For consistency, we have

used functions analogous to those defined in Ref. [14] to simplify our expression. The function $C_{pq}(z)$ is of the form

$$C_{pq}(z) \equiv (1-\gamma)^p(1+\gamma)^q \frac{\pi P_0 |U_0|^2}{|\beta|^2(\Delta\tilde{\beta})^p(\Delta\beta)^q}, \tag{3.14}$$

and accounts for many of the propagation constants of the beam. The function $F(\mathbf{r}_1, \mathbf{r}_2, z)$ has the form of a twisted GSM beam, and may be written as

$$\begin{aligned} F(\mathbf{r}_1, \mathbf{r}_2, z) =& exp[-N^2 r_1^2] exp[-\tilde{N}^2 r_2^2] exp[-M^2 |\mathbf{r}_2 - \mathbf{r}_1|^2] \\ & \times exp\left[\frac{2\pi i\alpha}{A^2|\beta|^2\Delta^2}\mathbf{r}_1 \wedge \mathbf{r}_2\right], \end{aligned} \tag{3.15}$$

where

$$N^2 \equiv \frac{\beta}{4\sigma^2\Delta^2 A^2|\beta|^2} - \frac{2\pi^2\alpha^2 z}{A^2|\beta|^2 i k_0 \Delta^2}, \tag{3.16}$$

$$M^2 \equiv \frac{1}{2A^2|\beta|^2}\left[\frac{1}{2\Delta^4} + 2\pi^2\alpha^2\right]. \tag{3.17}$$

We also combine a recurring set of expressions into the new term A^2, written as

$$A^2 \equiv \frac{1}{\Delta^2|\beta|^2} + \frac{4\pi^2\alpha^2 z^2}{k_0^2\Delta^2|\beta|^2} + \frac{1}{2\sigma^2}. \tag{3.18}$$

The vortex properties of the field manifest in the terms D_1 and D_2, written as

$$D_1(\mathbf{r}_1, \mathbf{r}_2) = \left[\frac{A^2}{1-i\gamma} - \frac{1}{2\Delta^2\tilde{\beta}} - \frac{\pi\alpha}{\tilde{\beta}}\right](x_1 - iy_1) - \left[\frac{1}{2\Delta^2\beta} - \frac{\pi\alpha}{\beta}\right](x_2 - iy_2), \tag{3.19}$$

$$D_2(\mathbf{r}_1, \mathbf{r}_2) = \left[\frac{A^2}{1+i\gamma} - \frac{1}{2\Delta^2\beta} - \frac{\pi\alpha}{\beta}\right](x_2 + iy_2) - \left[\frac{1}{2\Delta^2\tilde{\beta}} - \frac{\pi\alpha}{\tilde{\beta}}\right](x_1 + iy_1). \tag{3.20}$$

Our vtvGSM model beam has several important parameters we can use for tuning the total OAM and the spatial distribution of OAM in the beam. These consist of the wander parameter σ, the twist parameter α, the vortex orders m and n of the orthogonally polarized modes, and the polarization parameter Ψ.

The wander parameter has an inverse relationship to spatial coherence. This means that the fully coherent limit is $\sigma \to 0$, and as σ gets bigger the beam becomes less coherent. The wander parameter has an practical upper limit of $\sigma > \Delta$; once the wander parameter surpasses the width of the Gaussian envelope, the vortex properties of the field are effectively "washed out." Our main interest in this paper is the angular momentum, so the wander parameter will be set at a value indicative of partial coherence and remain largely unchanged.

It is important to note that the there is a strict upper limit to the twist parameter given by

$$\alpha_{max} = \frac{k_0}{2\pi\sigma}. \tag{3.21}$$

This limit reflects that the maximum tilt of any of our modes must have a transverse wavenumber smaller that the free-space wavenumber.

3.3 Total angular momentum flux density of vtvGSM beams

Now that we have the cross-spectral densities for each term in our cross-spectral density matrix as defined in Eq. (3.13), we can derive the total angular momentum flux density of our beam. This density is simply the sum of the total OAM density and the total SAM density, written as

$$M_{Total}(\mathbf{r}, z) = M_{OAM}(\mathbf{r}, z) + M_{SAM}(\mathbf{r}, z). \tag{3.22}$$

The OAM density satisfies the expression,

$$M_{OAM} = \frac{\epsilon_0}{2k_0}\mathrm{Im}\left\{\frac{\partial}{\partial\phi_2}\left[W_{mm}(\mathbf{r}_1, \mathbf{r}_2) + W_{nn}(\mathbf{r}_1, \mathbf{r}_2)\right]\right\}_{\mathbf{r}_1=\mathbf{r}_2=\mathbf{r}}, \tag{3.23}$$

and the SAM density satisfies the expression,

$$M_{SAM} = \frac{\epsilon_0}{2k_0}\mathrm{Im}\left[W_{mm}(\mathbf{r}_1, \mathbf{r}_2) - W_{nn}(\mathbf{r}_1, \mathbf{r}_2)\right]_{\mathbf{r}_1=\mathbf{r}_2=\mathbf{r}}. \tag{3.24}$$

We can use any non-negative values of m and n for our beams, giving us great flexibility in controlling the total OAM and the spatial distribution of OAM flux. Going forward, we choose $n = 0$, making one polarization component of the ensemble a Gaussian beam.

In Appendix A, we calculate the OAM flux density to be

$$\begin{aligned} M_{OAM} =& \frac{\epsilon_0}{2k_0} \exp\left[\frac{-r^2}{\sigma_S^2}\right] \Bigg\{ C_{00}(z)(1-\Psi)^2 \left[\frac{2\pi\alpha}{A^2|\beta|^2\Delta^2}\frac{1}{A^2} r^2\right] \\ & \times C_{mm}(z)\Psi^2 \left[\frac{2\pi\alpha}{A^2|\beta|^2\Delta^2} \sum_{k=0}^{m} a_k |Q|^{2(m-k)} r^{2(m-k+1)}\right. \\ & \left. + R \sum_{k=0}^{m} a_k (m-k)|Q|^{2(m-k-1)} r^{2(m-k)}\right] \Bigg\}. \end{aligned} \tag{3.25}$$

The expressions are quite long, and a number of constants have been defined to simply them. The quantities R and Q are defined by Eq. (3.40) and Eq. (3.41) respectively in Appendix A, and a_k is defined by Eq. (3.46) in the same Appendix.

As can be seen in Eq. (3.25), the OAM density has 3 distinct parts. The first term is the OAM associated with the twist of the right-hand circular component of the field. The second terms is the OAM associated with the twist of the left-hand circular component, and the third term is the OAM associated with the vortex phase of the left-hand circular component. The magnitude of these terms in the source plane is shown for a set of beam parameters in Figs. 3.1(a)-(c), and it can be seen that they are all significantly different.

There is also a direct SAM contribution to the total angular momentum. In Appendix B, we calculate the SAM density to be

$$\begin{aligned} M_{SAM} =& \Psi^2 \left[C_{mm}(z) exp\left[\frac{-r^2}{\sigma_S^2}\right] \sum_{k=0}^{m} a_k [|\tilde{G} - H|^2 r^2]^{m-k} \right] \\ & - (1-\Psi)^2 C_{00}(z) exp\left[\frac{-r^2}{\sigma_S^2}\right] \frac{1}{A^2}, \end{aligned} \tag{3.26}$$

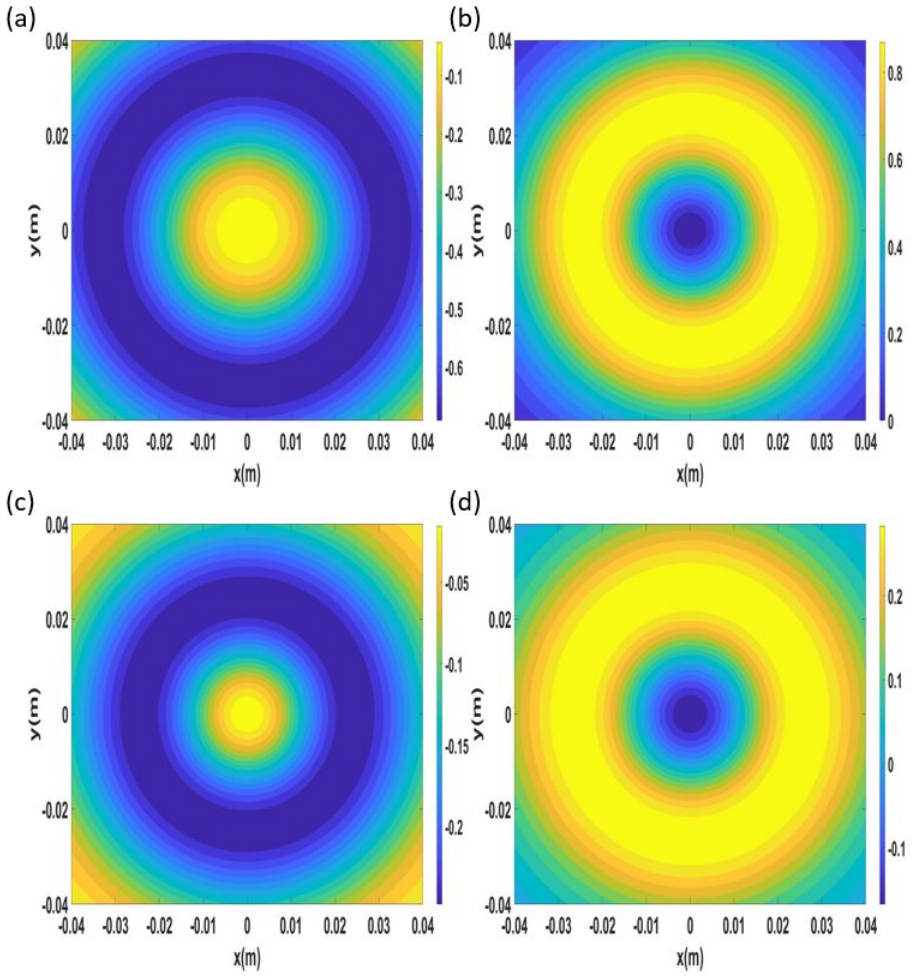

Figure 3.1: Cross-section plots of the OAM density shown in Eq. (3.25) and the SAM density shown in Eq. (3.26).These plots represent (a) the cross-term component of the OAM density, (b) the vortex order component of the OAM density, (c) the twist component of the OAM density and, (d) the total SAM density. Here $m = 1$, $\sigma = 0.01m$, $\Delta = 0.02m$, $\alpha = -800m^{-2}$ and $\Psi = 0.6$.

where G and H are also defined in Appendix A. A contour plot of this SAM density can be seen in Fig. 3.1(d), and it is distinct from the OAM contributions.

With multiple degrees of freedom in the design of our beam, we have the capability to create interesting beam behavior through a careful choice of parameters. One possibility is the creation of counter-rotating regions within the beam's cross-section. In Ref. [19], it was shown that partially coherent beams can be created where the OAM is tailored to produce counter-rotating regions. In Fig. 3.2, we show an example

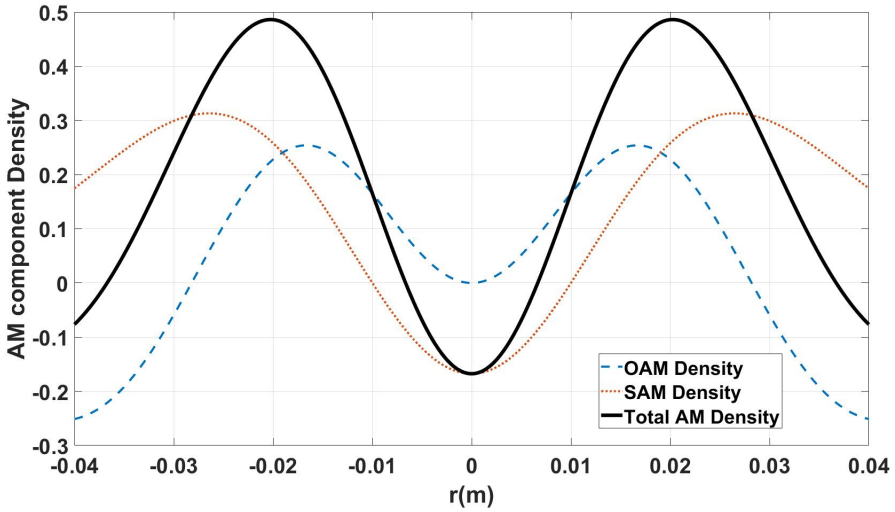

Figure 3.2: The OAM density, SAM density, and total angular momentum density of a counter-rotating beam. Here $m = 1$, $n = 0$, $\sigma = 0.01m$, $\Delta = 0.02m$, $\alpha = -800m^{-2}$ and $\Psi = 0.6$.

of a beam where the OAM density and SAM density are combined to produce counter-rotation. The SAM density near the center of the beam is negative, while the OAM density is positive. The total AM density is negative near the beam core, but positive in the immediate outskirts of the beam.

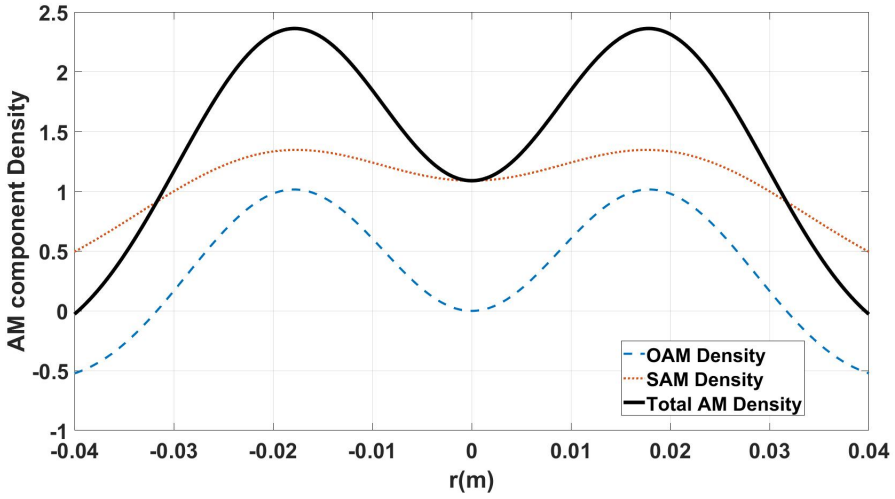

Figure 3.3: The OAM density, SAM density, and total angular momentum density of a beam with a positive angular momentum density core. Here $m = 1$, $n = 0$, $\sigma = 0.01m$, $\Delta = 0.02m$, $\alpha = -1000m^{-2}$ and $\Psi = 0.9$.

SAM provides additional flexibility that OAM alone does not. Referring back to Eq. (3.25), it is to be noted that the OAM flux density has a radial dependence near the origin with lowest order r^2. In the center of the beam, there is no angular momentum flux; this is a potential problem for trapping and rotation applications. The SAM flux density has a non-zero component at the origin, however, allowing us to create a positive total angular momentum density core. An example of this total flux is shown in Fig. 3.3.

3.4 Angular momentum flux density per photon

The angular momentum flux density considered so far depends not only on the strength of circulation of the beam but also the local intensity of the beam (photon flux): the more photons that are present in a location, the stronger the flux density will be. It is of physical interest, however, to investigate the circulation inherent to the beam structure by normalizing out the beam intensity. We may define the angular momentum flux density per photon as

$$m_z(\mathbf{r}, z) = \hbar\omega \frac{M_{total}(\mathbf{r}, z)}{S_z(\mathbf{r}, z)}, \tag{3.27}$$

where $S_z(\mathbf{r}, z)$ is the z-component of the Poynting vector, which takes on the form

$$S_z(\mathbf{r}, z) = \frac{k_0}{\mu_0 \omega} Re\{W_{mm} + W_{nn}\}_{\mathbf{r}_1=\mathbf{r}_2=\mathbf{r}}. \tag{3.28}$$

For our case, with $n = 0$, the Poynting vector is

$$S_z(\mathbf{r}, z) = \exp\left[\frac{-r^2}{\sigma_S^2}\right] \left[C_{mm}(z) \sum_{k=0}^{m} \left[a_k |Q|^{2(m-k)} r^{2(m-k)}\right] + \frac{C_{00}(z)}{A^2}\right]. \tag{3.29}$$

A striking result of Ref. [14] was the demonstration that it is possible to create a "dead zone" in the core of a tvGSM beam by canceling out the r^2 terms from the two sources of OAM. For vtvGSM beams, we can go a step further and use SAM to

create a more intense dead zone by canceling out both the r^2 and r^4 terms of the total angular momentum, leaving the total AM depending on r^6. To do so, we must use a vortex order of $m = 2$ in order to even have an r^6 term.

We organize the terms of Eqs. (3.25) and (3.26) in powers of r^2. We consider the form of m_z in the immediate neighborhood of the origin, where the Gaussian envelope of the beam may be neglected. This gives the lengthy approximation for the angular momentum density per photon,

$$\begin{aligned} m_z = &\left[\Psi^2 C(z)\frac{2\pi\alpha}{A^2|\beta|^2\Delta^2}\frac{(m-1)m(m!)}{4A^{2m+6}}|Q|^4\right] r^6 \\ &+ \left[\Psi^2\frac{2\pi\alpha}{A^2|\beta|^2\Delta^2}\frac{m(m!)}{A^{2m+4}}|Q|^2 + \Psi^2 R\frac{(m-1)m(m!)}{4A^{2m+6}}|Q|^2\right. \\ &\left.+ \Psi^2\frac{(m-1)m(m!)}{4A^{2m+6}}[(\tilde{G}-H)(G-\tilde{H})]^2\right] C(z) r^4 \\ &+ \left[\Psi^2 C(z)\frac{2\pi\alpha}{A^2|\beta|^2\Delta^2}\frac{m!}{A^{2m+2}} + (1-\Psi)^2 C_0(z)\frac{6\pi\alpha}{A^2|\beta|^2\Delta^2}\frac{1}{A^2}\right. \\ &\left.+ \Psi^2 C(z) R\frac{m(m!)}{A^{2m+4}} + \Psi^2 C(z)\frac{m(m!)}{A^{2m+4}}(\tilde{G}-H)(G-\tilde{H})\right] r^2 \\ &+ \Psi^2 C(z)\frac{m!}{A^{2m+2}} - (1-\Psi)^2 C_0(z)\frac{3}{A^2}. \end{aligned} \tag{3.30}$$

For clarity, the denominator containing the Poynting vector, Eq. (3.29), has been omitted; near the origin, the Poynting vector will be approximately constant.

An important feature of this equation is that there are two r^0 terms at its end. This has a direct impact that can be seen when we begin zeroing the other groups in the approximation. To create a dead zone, we have three independent parameters: the vortex order m, the twist parameter α, and the polarization amplitude coefficient Ψ. Our initial goal is to zero out all terms excluding the r^6 group; as already noted, this requires a vortex order of $m = 2$. We then vary the twist parameter and the polarization amplitude coefficient to manipulate the strength of the r^4 and r^2 groups. In Fig. 3.4, we plot the total angular momentum of the r^4 against a range of twist parameters and select the point at which the total angular momentum is zero, in this

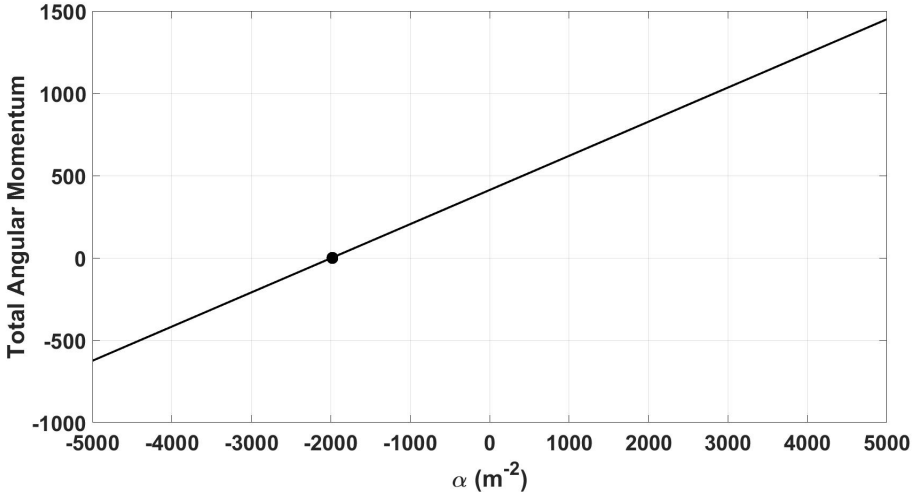

Figure 3.4: The total angular momentum of the r^4 term in Eq. 3.30 as a function of α. Here $m = 2$, $\sigma = .01m$, $\Delta = .02m$ and $\Psi = .5$.

case it is at $\alpha = -1989.4m^{-2}$. This process is repeated for the r^2 grouping but instead of the twist parameter we find the polarization amplitude coefficient that will zero this group. In Fig. 3.4, the initial chosen value of Ψ must fall within $0 < \Psi \leq 1$. Different values of Ψ within this range have negligible impacts of the value of α required to zero the r^4 approximation term. Thus the subsequent zeroing of the r^2 term and the plot shown in Fig. 3.5 are effectively unchanged with different values of initial Ψ.

In Fig. 3.5, we can see that there is a significant flat region of the angular momentum density in the core. However, it is not a complete "dead zone" because of the aforementioned two r^0 terms. These two terms are unable to be canceled out with the r^2 and r^4 terms and thus there will always be zone of non-zero angular momentum density per photon in the core. However; we are able to create a consistent "near-dead zone" of circulation around the core of the beam. This is a natural expansion of what was accomplished in Ref. [14]. This behavior clearly demonstrates that it that is is possible to control both the total angular momentum in partially coherent beams as well as its transverse distribution.

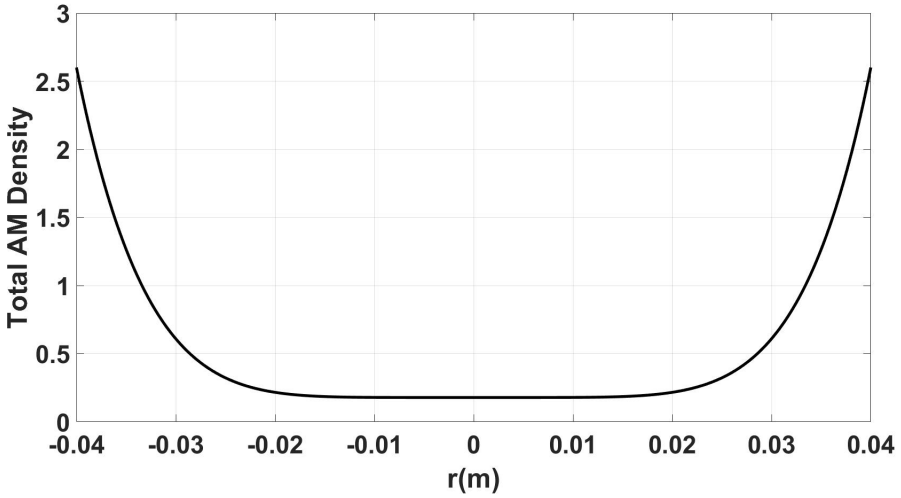

Figure 3.5: The local angular momentum density per photon as presented in Eq. (3.30) with r^2 and r^4 terms zeroed. Here $m = 2$, $\alpha = -1989.4m^{-2}$, and $\Psi = .565$.

3.5 Practical considerations

The vtvGSM beams provide significant control over the transverse angular moment of the beam, at the cost of significant beam complexity. It is worthwhile to give an example of how this beam can be generated, at least in principle.

In Fig. 3.6, we propose an experimental optics scheme that will produce the vtvGSM beam explored in this paper. The scheme begins with a coherent source incident on a polarizer such that it has an even distribution of horizontal and vertical polarization. This polarized beam is then split and propagated along separate paths, each component passing through quarter-wave plates oriented to produce circular polarizations of either handedness. We then use a spiral phase plate along one path to impart the vortex order upon the beam.

Once the beams are recombined we have a vector vortex beam, but the partial coherence effects must still be imposed. To experimentally produce a tGSM, we follow the techniques outlined in Ref. [20]. The first step it to convert the beam into an anisotropic Gaussian-Schell model beam (AGSM). A partially coherent illuminating field of Schell-model form resembling Eq. (3.2) is created by passing the light through

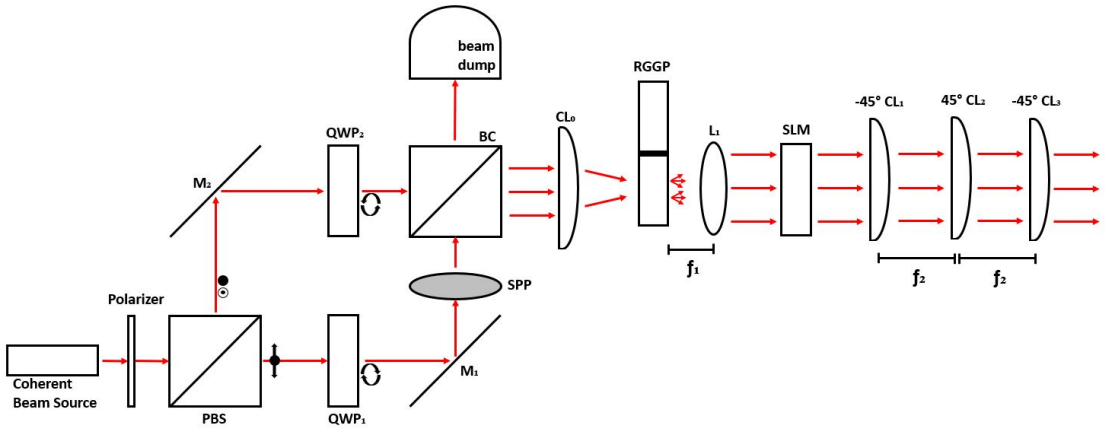

Figure 3.6: An experimental scheme to produce the proposed vtvGSM beam. PBS, polarized beam splitter; QWP_1,QWP_2, quarter-wave plate; M_1, M_2, reflecting mirror; SPP, spiral phase plate; BC, beam combiner; RGGP, rotating ground glass plate; L_1, thin lens; SLM, spatial light modulator; CL_1, CL_2, CL_3, CL_4, cylindrical thin lenses.

an off-axis rotating ground glass plate (RGGP) at the Fourier plane of a lens [21,22]. Thus by focusing the beam onto the RGGP with a cylindrical lens we create a partially coherent beam with an elliptically anisotropic Gaussian degree of coherence. The collimated beam then propagates through the spatial light modulator (SLM) which converts the intensity profile to an elliptical Gaussian shape. This procedure yields a controlled AGSM beam. To impart the twist we utilize a 3 cylindrical lens system. CL_1 and CL_3 form a 4f imaging system and CL_2 performs a Fourier transform in an orthogonal direction with respect to CL_1. All of this combined produces a vtvGSM beam with the degrees of freedom discussed in this paper.

This system is quite elaborate, and is provided as a proof of feasibility for generating vtvGSM beams; it is likely possible to come up with simpler experimental configurations to produce such beams.

3.6 Conclusion

We have demonstrated how to generalize the class of twisted vortex Gaussian Schell-model beams to create beams that also possess non-trivial spin angular momentum, called vector twisted vortex Gaussian Schell-model beams. It was shown that with

the addition of this new degree of freedom, one can produce beams with unusual angular momentum structures, including beams with counter-rotating regions, beams with appreciable angular momentum at the core, and beams with angular momentum "dead zones." These results extend the understanding of angular momentum in optical beams and provide additional control of angular momentum for applications.

REFERENCES

[1] G.J. Gbur. *Singular Optics*. CRC Press, 2017.

[2] Marat Soskin, Svetlana V Boriskina, Yidong Chong, Mark R Dennis, and Anton Desyatnikov. Singular optics and topological photonics. *Journal of Optics*, 19(1):010401, dec 2016.

[3] Mark R. Dennis, Kevin O'Holleran, and Miles J. Padgett. Chapter 5 singular optics: Optical vortices and polarization singularities. volume 53 of *Progress in Optics*, pages 293-363. Elsevier, 2009.

[4] Jian Wang. Advances in communications using optical vortices. *Photon. Res.*, 4(5):B14-B28, Oct 2016.

[5] Greg Gbur and Robert K. Tyson. Vortex beam propagation through atmospheric turbulence and topological charge conservation. *J. Opt. Soc. Am.* A, 25(1):225-230, Jan 2008.

[6] Yingqi Liao, Suhui Yang, Kun Li, Junwen Ji, Xuetong Lin, Yan Hao, Zhuo Li, Xin Wang, and Jinying Zhang. Reduction of scattering clutters in an underwater lidar system by using an optical vortex. *IEEE Photonics Technology Letters*, 34(17):927-930, 2022.

[7] Austin Jantzi, William Jemison, Alan Laux, Linda Mullen, and Brandon Cochenour. Enhanced underwater ranging using an optical vortex. *Opt. Express*, 26(3):2668-2674, Feb 2018.

[8] N. B. Simpson, K. Dholakia, L. Allen, and M. J. Padgett. Mechanical equivalence of spin and orbital angular momentum of light:an optical spanner. *Opt. Lett.*, 22(1):52-54, Jan 1997.

[9] Graham Gibson, Johannes Courtial, Miles J. Padgett, Mikhail Vasnetsov, Valeriy Pas'ko, Stephen M. Barnett, and Sonja Franke-Arnold. Free-space information transfer using light beams carrying orbital angular momentum. *Opt. Express*, 12(22):5448-5456, Nov 2004.

[10] Jaime A. Anguita, Mark A. Neifeld, and Bane V. Vasic. Turbulence-induced channel crosstalk in an orbital angular momentum-multiplexed free-space optical link. *Appl. Opt.*, 47(13):2414-2429, May 2008.

[11] Greg Gbur. Partially coherent beam propagation in atmospheric turbulence. *J. Opt. Soc. Am.* A, 31(9):2038-2045, Sep 2014.

[12] Franco Gori and Massimo Santarsiero. Twisted Gaussian Schell-model beams as series of partially coherent modified Bessel-Gauss beams. *Optics letters*, 40 7:1587-90, 2015.

[13] C. S. D. Stahl and G. Gbur. Partially coherent vortex beams of arbitrary order. *J. Opt. Soc. Am.* A, 34(10):1793-1799, Oct 2017.

[14] C. S. D. Stahl and G. Gbur. Twisted vortex Gaussian Schell-model beams. *J. Opt. Soc. Am.* A, 35(11):1899-1906, Nov 2018.

[15] G. Gbur. Partially coherent vortex beams. In E.J. Galvez and D.L. Andrews, editors, *Proc. SPIE*, volume 10549, page 1054903. SPIE, 2018.

[16] L. Mandel and E. Wolf. *Optical Coherence and Quantum Optics*. Cambridge University Press, 1995.

[17] G.Gbur, T.D. Visser, and E. Wolf. hidden singularities in partially coherent wavefields. *Journal of Optics A:Pure and Applied Optics*, 6(5):S239-S242, apr 2004.

[18] Emil Wolf. *Introduction to the theory of coherence and polarization of light.* Cambridge University Press, 2007.

[19] Yongtao Zhang, Yangjian Cai, and Greg Gbur. Control of orbital angular momentum with partially coherent vortex beams. *Opt. Lett.*, 44(15):3617-3620, Aug 2019.

[20] Haiyun Wang, Xiaofeng Peng, Lin Liu, Fei Wang, Yangjian Cai, and Sergey A. Ponomarenko. Generating bona fide twisted gaussian schell-model beams. *Opt. Lett.*, 44(15):3709-3712, Aug 2019.

[21] Y. Gu and G. Gbur. Topological reactions of optical correlation vortices. *Optics Communications*, 282(5):709-716, 2009.

[22] Toshimitsu Asakura. Spatial coherence of laser light passed through rotating ground glass. *Opto-electronics*, 2:115-123, 1970.

APPENDIX A: OAM Density Calculation

The z component of the OAM density can be expressed as

$$M_{OAM} = \frac{\epsilon_0}{k_0} Im \left[\frac{\partial}{\partial \phi_2} W(\mathbf{r}_1, \mathbf{r}_2) \right]_{r_1 = r_2 = r}, \tag{3.31}$$

where $W(\mathbf{r}_1, \mathbf{r}_2) = W_{mm}$ as shown in Eq. (3.13). For mathematical convenience, we first convert everything into polar coordinates. Beginning with the properties of the vortex as shown in Eq. (3.19) and Eq.(3.20). When converted they can be written as

$$D_1 = \tilde{G}(\rho_1 exp[-i\phi_1]) - H(\rho_2 exp[-i\phi_2]), \tag{3.32}$$

$$D_2 = G(\rho_2 exp[i\phi_2]) - \tilde{H}(\rho_1 exp[i\phi_1]), \tag{3.33}$$

where

$$G = \frac{A^2}{1 + i\gamma} - \frac{1}{2\Delta^2 \beta} - \frac{\pi \alpha}{\beta}, \tag{3.34}$$

and

$$H = \frac{1}{2\Delta^2 \beta} - \frac{\pi \alpha}{\beta}. \tag{3.35}$$

The combined term of the properties, as shown in W_{mm} in Eq. (3.13) is defined as

$$\begin{aligned} (D_1 D_2)^{m-k} = \Big[& |G|^2 \rho_1 \rho_2 exp[i(\phi_2 - \phi_1)] \\ & + |H|^2 \rho_1 \rho_2 exp[i(\phi_1 - \phi_2)] - \tilde{G}\tilde{H}\rho_1^2 - GH\rho_2^2 \Big]^{(m-k)}. \end{aligned} \tag{3.36}$$

The polar for of the function representing the twisted Gaussian-Schell model beam

can be written as

$$F(\mathbf{r}_1, \mathbf{r}_2, z) = exp\left[-N^2\rho_1^2 - \tilde{N}^2\rho_2^2 - M^2\rho_1^2 - M^2\rho_2^2\right] exp\left[M^2 2(\rho_2\rho_1 cos(\phi_2 - \phi_1))\right] \times exp\left[\frac{i2\pi\alpha}{A^2|\beta|^2\Delta^2}\rho_2\rho_1 sin(\phi_1 - \phi_2)\right]. \tag{3.37}$$

Thus the polar form of the cross-spectral density term W_{mm} is

$$W(\rho_1, \rho_2) = \Psi^2 C_{mm}(z) exp\left[-N^2\rho_1^2 - \tilde{N}^2\rho_2^2 - M^2\rho_1^2 - M^2\rho_2^2\right] \times exp\left[(\frac{i2\pi\alpha}{A^2|\beta|^2\Delta^2}\rho_2\rho_1 sin(\phi_1 - \phi_2)) + (M^2 2\rho_2\rho_1 cos(\phi_2 - \phi_1))\right] \times \sum_{k=0}^{m} a_k\left[|G|^2\rho_1\rho_2 exp[i(\phi_2 - \phi_1)] + |H|^2\rho_1\rho_2 exp[i(\phi_1 - \phi_2)] - \tilde{G}\tilde{H}\rho_1^2 - GH\rho_2^2\right]^{(m-k)} \tag{3.38}$$

Now take the partial derivative with respect to ϕ_2. we use the product rule on the last two terms. Once the partial derivative is complete, we set $r_1 = r_2 = r$ and simplify the cross-spectral density to be of the form

$$\frac{\partial}{\partial\phi_2}W(\mathbf{r}_1, \mathbf{r}_2) = \Psi^2 C_{mm}(z) exp\left[\frac{-r^2}{\sigma_S^2}\right] \times \left[iR\sum_{k=0}^{m} a_k(m-k)|Q|^{2(m-k-1)}r^{2(m-k)} + \frac{i2\pi\alpha}{A^2|\beta|^2\Delta^2}\sum_{k=0}^{m} a_k|Q|^{2(m-k)}r^{2(m-k+1)}\right]. \tag{3.39}$$

where:

$$R = |G|^2 - |H|^2, \tag{3.40}$$

and

$$Q = \frac{1}{1 - i\gamma}\frac{1}{2\sigma^2}, \tag{3.41}$$

and

$$\sigma_S^2 = 2\sigma^2 + \Delta^2 \left(\frac{8\pi^2\alpha^2\sigma^2}{k_0^2} + \frac{1}{k_0^2\Delta^2} \right) z^2. \tag{3.42}$$

Taking the imaginary component gives the Orbital angular momentum density, written as

$$\begin{aligned} M_{OAM-mm} =& \Psi^2 \frac{\epsilon_0}{k_0} C_{mm}(z) exp\left[\frac{-r^2}{\sigma_S^2}\right] \\ & \times \left[\frac{2\pi\alpha}{A^2|\beta|^2\Delta^2} \sum_{k=0}^{m} a_k |Q|^{2(m-k)} r^{2(m-k+1)} \right. \\ & \left. + R \sum_{k=0}^{m} a_k (m-k) |Q|^{2(m-k-1)} r^{2(m-k)} \right]. \end{aligned} \tag{3.43}$$

For the diagonal terms, set the OAM to the special case of $m = 0$, this gives

$$M_{OAM-00} = \frac{\epsilon_0}{k_0}(1-\Psi)^2 C_{00}(z) exp\left[\frac{-r^2}{\sigma_S^2}\right] \left[\frac{2\pi\alpha}{A^2|\beta|^2\Delta^2}\frac{1}{A^2} r^2\right]. \tag{3.44}$$

Combining what was calculated previously gives total OAM density, written as

$$\begin{aligned} M_{OAM} =& \frac{\epsilon_0}{2k_0} exp\left[\frac{-r^2}{\sigma_S^2}\right] \left\{ C_{mm}(z) \right. \\ & \times \Psi^2 \left[\frac{2\pi\alpha}{A^2|\beta|^2\Delta^2} \sum_{k=0}^{m} a_k |Q|^{2(m-k)} r^{2(m-k+1)} \right. \\ & \left. + R \sum_{k=0}^{m} a_k (m-k) |Q|^{2(m-k-1)} r^{2(m-k)} \right] \\ & \left. + C_{00}(z)(1-\Psi)^2 \left[\frac{2\pi\alpha}{A^2|\beta|^2\Delta^2}\frac{1}{A^2} r^2 \right] \right\}, \end{aligned} \tag{3.45}$$

where:

$$a_k = \binom{m}{k}^2 \frac{\Gamma(k+1)}{A^{4m-2k+2}}. \tag{3.46}$$

APPENDIX B: SAM Density Calculation

The spin angular momentum for a circular polarization can be defined as

$$lm\left[< E_x^* E_y > - < E_y^* E_x >\right], \tag{3.47}$$

where

$$E_x = \frac{E_+ + E_-}{\sqrt{2}}, E_y = \frac{E_+ - E_-}{\sqrt{2}}. \tag{3.48}$$

Combining the above two equations and expanding, the SAM becomes

$$lm\left[\frac{1}{2i}(E_+^* + E_-^*)(E_+ - E_-) + \frac{1}{2i}(E_+^* - E_-^*)(E_+ + E_-)\right] \tag{3.49}$$

Converting this to be in terms of the cross-spectral density defines the SAM to be written as

$$M_{SAM} = Im[E_+^* E_+ - E_-^* E_-] = Im\left[W_{mm}(\mathbf{r}_1, \mathbf{r}_2) - W_{nn}(\mathbf{r}_1, \mathbf{r}_2)\right]. \tag{3.50}$$

Plugging in the cross-spectral densities as defined in Eq. (3.13) and simplifying the twisted Gaussian-Schell model beam function gives the total SAM density, shown to be

$$\begin{aligned} M_{SAM} =& \Psi^2 \left[C_{mm}(z) exp\left[\frac{-r^2}{\sigma_S^2}\right] \sum_{k=0}^{m} a_k [|\tilde{G} - H|^2 r^2]^{m-k} \right] \\ & - (1-\Psi)^2 C_{00}(z) exp\left[\frac{-r^2}{\sigma_S^2}\right] \frac{1}{A^2}, \end{aligned} \tag{3.51}$$

CONCLUSION

In this dissertation we investigated the properties and uses of structured light under partially coherent conditions. Specifically we studied the properties of partially coherent vortex beams, such as the total angular momentum, and investigated the effects of partial coherence on vortex created superoscillations. We explored the effect of partial coherence on this superoscillatory behavior through several different models, and demonstrated that it is possible in some cases for a decrease in coherence to decrease the spacing of superoscillatory zeros and consequently increase the strength of superoscillations. It was also shown that since the zeros manifest in the two-point cross-spectral density instead of the spectral density of the field, the rapid oscillations of the superoscillatory phase can be seen even in locations where there is appreciable light intensity. This could provide a possible mechanism to overcome the low light limitation of coherent superoscillation based imaging systems, such as in superoscillatory lenses [25].

We further explored partially coherent superoscillatory fields by utilizing the Talbot effect. The manipulation of spatial coherence in the superoscillatory Talbot effect provides new degrees of freedom for manipulating the strength of superoscillations. This further supported our previous findings that showed superoscillatory behavior increasing in strength as the spatial coherence decreased. For the Talbot effect case, this corresponded to the zeros of the cross-spectral density moving closer together and eventually annihilating. When this annihilation occurs, the superoscillatory behavior subsequently disappeared. In both Chapter 1 and Chapter 2, we have seen that changes in both the spatial coherence and the observation point can dramatically affect the superoscillatory behavior. The combination of these two adjustable factors provides great flexibility in tailoring these superoscillations for applications.

All of these aforementioned results have been explored with an eye towards using partially coherent superoscillations in imaging applications. The possibility of having

appreciable intensity in the region of superoscillations is an exciting revelation that makes incorporating superoscillations much more practical. It is to be noted that an imaging system based on partially coherent superoscillations would need to be very different from a conventional imaging system, due to the use of the two-point correlation function. Sensing schemes which take advantage of interferometry to image objects and otherwise detect their structure could potentially benefit from such partially coherent superoscillations.

Additionally, we explored the inclusion of polarization to the class of partially coherent vortex beams known as Twisted Vortex Gaussian-Schell Model Beams. It was shown that with the addition of this new degree of freedom we have great control over the angular momentum characteristics of the beam, including the creation of "dead zones" in the core, the creation of counter-rotating beams, and the production of beams with appreciable angular momentum cores. This unprecedented control could be a boon for applications that require precise manipulation of a beam's transverse distribution of angular momentum, such as optical tweezing or encoding information in different angular momentum modes for optical communications.

For the continuation of this research, one of the natural next steps would be to experimentally demonstrate the practical optics schemes proposed in Chapter 1 and Chapter 3. These schemes would produce the fields outlined in those chapters. The optical scheme in Chapter 3 would allow for experimental production of the angular momentum control demonstrated in that paper for comparison. The construction and characterization of such a system would require intensive analysis and testing of every optical component. This is to assure that uncertainty introduced is minimal enough that the control of the the beam characteristics discussed is not made ineffective. Unfortunately, even though we would be able to produce the desired field detailed in Chapter 1, in order to practically image the fields, a non-conventional system would need to be used as discussed previously. Thus a further exploration in the develop-

ment of a sensing scheme that could observe the phase of the correlation function is required. This is likely to be an interferometric scheme, and an investigation into how such a system could be implemented and any benefits it might provide is a necessity for future imaging applications. Further investigation into a radial variation of our modal coherence model outlined in Chapter 1 could lead to sub-wavelength spot sizes that remain or get smaller when the field is randomized, thus having direct impact on superoscillatory imaging applications. Our work on the partially coherent superoscillatory Talbot effect gives us insight into the expected features of the imaging field. Our main focus was the behavior of superoscillations in a partially coherent Talbot carpet. There are several aspects of our field that could be expanded upon. These include how a limited grating size would impact the behavior, the behavior at specific Talbot distances containing doubled images, and the use of a multi-dimensional grating. We utilized a one-dimensional grating, thus the natural progression of this project would include the development of a two-dimensional grating that produces the similar effects seen throughout Chapter 2. This would require defining a quasi-periodic grating that produces a Talbot-like effect and supports the superoscillations produced by the input field [28, 29]. The simulation of this quasi-periodic grating could then be experimentally tested through the construction of a precisely machined physical counterpart. This would then open exploration into how a repeated field of multiple superoscillations behaves under different conditions. These projects will help push the boundaries of the current knowledge of partially coherent structured light, enabling exciting prospects for imaging, communications, and other applications yet to be imagined.

REFERENCES

[1] Jian Wang. Advances in communications using optical vortices. *Photon. Res.*, 4(5):B14–B28, Oct 2016.

[2] Jae Hoon Lee, Gregory Foo, Eric G. Johnson, and Grover A. Swartzlander. Experimental verification of an optical vortex coronagraph. *Phys. Rev. Lett.*, 97:053901, Aug 2006.

[3] David Palacios, David Rozas, and Grover A. Swartzlander. Observed scattering into a dark optical vortex core. *Phys. Rev. Lett.*, 88:103902, Feb 2002.

[4] Austin Jantzi, William Jemison, Alan Laux, Linda Mullen, and Brandon Cochenour. Enhanced underwater ranging using an optical vortex. *Opt. Express*, 26(3):2668–2674, Feb 2018.

[5] N. B. Simpson, K. Dholakia, L. Allen, and M. J. Padgett. Mechanical equivalence of spin and orbital angular momentum of light:an optical spanner. *Opt. Lett.*, 22(1):52–54, Jan 1997.

[6] Graham Gibson, Johannes Courtial, Miles J. Padgett, Mikhail Vasnetsov, Valeriy Pas'ko, Stephen M. Barnett, and Sonja Franke-Arnold. Free-space information transfer using light beams carrying orbital angular momentum. *Opt. Express*, 12(22):5448–5456, Nov 2004.

[7] M. Berry, N. Zheludev, Y. Aharonov, F. Colombo, I. Sabadini, D.C. Struppa, J. Tollaksen, E.T.F. Rogers, F. Qin, M. Hong, X. Luo, R. Remez, A. Arie, J.B. Götte, M.R. Dennis, A.M.H. Wong, G.V. Eleftheriades, Y. Eliezer, A. Bahabad, G. Chen, Z. Wen, G. Liang, C. Hao, C-W Qiu, A. Kempf, E. Katzav, and M. Schwartz. Roadmap on superoscillations. *Journal of Optics*, 21(5):053002, apr 2019.

[8] G. Gbur. Using superoscillations for superresolved imaging and subwavelength focusing. *Nanophotonics*, 8(2):205 – 225, 01 Feb. 2019.

[9] I. Chremmos and G. Fikioris. Superoscillations with arbitrary polynomial shape. *Journal of Physics A: Mathematical and Theoretical*, 48(26):265204, jun 2015.

[10] A.M.H. Wong and G.V. Eleftheriades. Sub-wavelength focusing at the multi-wavelength range using superoscillations: an experimental demonstration. *IEEE Trans. Antenn. Propag.*, 59:4766–4776, 2011.

[11] E.T.F. Rogers, J. Lindberg, T. Roy, S. Savo, J.E. Chad, M.R. Dennis, and N.I. Zheludev. A super-oscillatory lens optical microscope for subwavelength imaging. *Nature Materials*, 11:432–435, 2012.

[12] E.T.F. Rogers, S. Savo, J. Lindberg, T. Roy, M.R. Dennis, and N.I. Zheludev. Super-oscillatory optical needle. *Appl. Phys. Lett.*, 102:031108, 2013.

[13] T. Roy, E.T.F. Rogers, G. Yuan, and N.I. Zheludev. Point spread function of the optical needle super-oscillatory lens. *Appl. Phys. Lett.*, 104:231109, 2014.

[14] M.K. Smith and G. Gbur. Mathematical method for designing superresolution lenses using superoscillations. *Opt. Lett.*, 45(7):1854–1857, Apr 2020.

[15] Yoon Bae, Martin Sohn, Dong-Ryoung Lee, and Sang-Soo Choi. Effect of partial coherence on dimensional measurement sensitivity for duv scatterfield imaging microscopy. (27), 2019-10-02 00:10:00 2019.

[16] W. S. C. Chang and N. R. Kilcoyne. A study of partial coherence and its application to the collimation of pulsed multimode laser radiation. *Appl. Opt.*, 4(11):1404–1411, Nov 1965.

[17] Greg Gbur. Partially coherent beam propagation in atmospheric turbulence [invited]. *J. Opt. Soc. Am. A*, 31(9):2038–2045, Sep 2014.

[18] M.V. Berry. Suppression of superoscillations by noise. *Journal of Physics A: Mathematical and Theoretical*, 50(2):025003, dec 2016.

[19] E. Katzav, E. Perlsman, and M. Schwartz. Yield statistics of interpolated superoscillations. *Journal of Physics A: Mathematical and Theoretical*, 50(2):025001, dec 2016.

[20] I.D. Maleev, D.M. Palacios, A.S. Marathay, and G.A. Swartzlander, Jr. Spatial correlation vortices in partially coherent light: theory. *J. Opt. Soc. Am. B*, 21:1895–1900, 2004.

[21] D.M. Palacios, I.D. Maleev, A.S. Marathay, , and Jr. G.A. Swartzlander. Spatial correlation singularity of a vortex field. *Phys. Rev. Lett.*, 92:143905, 2004.

[22] Emil Wolf. *Introduction to the theory of coherence and polarization of light.* Cambridge University Press, 2007.

[23] G.Gbur, T.D. Visser, and E. Wolf. hidden singularities in partially coherent wavefields. *Journal of Optics A: Pure and Applied Optics*, 6(5):S239–S242, apr 2004.

[24] M V Berry and S Popescu. Evolution of quantum superoscillations and optical superresolution without evanescent waves. *Journal of Physics A: Mathematical and General*, 39(22):6965–6977, may 2006.

[25] Gang Chen, Zhong-Quan Wen, and Cheng-Wei Qiu. Superoscillation: from physics to optical applications. *Light: Science & Applications*, 8(1):56, 2019.

[26] Greg Gbur and Robert K. Tyson. Vortex beam propagation through atmospheric turbulence and topological charge conservation. *J. Opt. Soc. Am. A*, 25(1):225–230, Jan 2008.

[27] C. S. D. Stahl and G. Gbur. Twisted vortex Gaussian Schell-model beams. *J. Opt. Soc. Am. A*, 35(11):1899–1906, Nov 2018.

[28] Fu Min Huang, Yifang Chen, F Javier Garcia de Abajo, and Nikolay I Zheludev. Optical super-resolution through super-oscillations. *Journal of Optics A: Pure and Applied Optics*, 9(9):S285, aug 2007.

[29] Chong Zhang, Wei Zhang, Furui Li, Junhong Wang, and Shuyun Teng. Talbot effect of quasi-periodic grating. *Appl. Opt.*, 52(21):5083–5087, Jul 2013.